

On recovering of distributed IP parameters in time domain electromagnetic data

Seogi Kang

December 1, 2015

Contents

1	Introduction	2
2	Backgrounds	2
2.1	Complex conductivity	2
2.2	Convolution approach	3
2.3	Decomposition of EM responses	6
2.4	Thoughts on IP and polarization currents	7
3	Linearization of IP responses	8
3.1	Linearization in EIP and MIP	8
3.2	Linearization in TEM-IP	10
3.3	Discussions	12
3.3.1	Choice of reference electric field	12
3.3.2	Revisitation of EIP and MIP	14
3.3.3	Ignoring inductive IP effect	15
4	IP inversion methodology	16
4.1	IP inversion procedure	16
4.2	An equivalent pseudo-chargeability	16
4.3	3D IP inversion with linearized kernel	17
5	Application: airborne time domain EM	18
5.1	Analyses of ATEM-IP responses	20
5.2	Analyses of IP currents	25
5.3	Validation of linearization	26
5.3.1	IP current	26
5.3.2	IP response	34
5.3.3	Discussion for the resistive case	35
5.4	A potential for recovering IP parameters	37
5.4.1	Validation for an equivalent pseudo-chargeability	37
5.4.2	Depth weight and positivity on pseudo-chargeability	42
5.4.3	Incorrect conductivity mode with positivity constraint	44
5.4.4	Extracting intrinsic IP parameters	48

1 Introduction

2 Backgrounds

2.1 Complex conductivity

An often-used representation for complex conductivity in the frequency domain is the Cole-Cole model [2]:

$$\sigma(\omega) = \sigma_\infty - \sigma_\infty \frac{\eta}{1 + (1 - \eta)(i\omega\tau)^c} = \sigma_\infty + \Delta\sigma(\omega), \quad (1)$$

where σ_∞ is the conductivity at infinite frequency, η is the intrinsic chargeability, τ is the time constant and c is the frequency dependency. Real and imaginary parts of complex conductivity in frequency domain are shown in Figure 1(a) with Cole-Cole parameters: $\sigma_\infty = 10^{-2}$ S/m, $\eta = 0.5$, $\tau = 0.01$ and $c=1$. By applying inverse Fourier transform with time dependency, $e^{i\omega t}$, we have

$$\sigma(t) = \mathcal{F}^{-1}[\sigma(\omega)] = \sigma_\infty\delta(t) + \Delta\sigma(t) \quad (2)$$

where $\delta(t)$ is Dirac delta function and $\mathcal{F}^{-1}[\cdot]$ is inverse Fourier transform operator. Computation of $\Delta\sigma(t)$ can be convenient by assuming $c = 1$, which is usually called Debye model. By evaluating inverse Fourier transform of $\Delta\sigma(\omega)$ when $c = 1$, we have

$$\sigma(t) = \sigma_\infty\delta(t) - \sigma_\infty\tilde{\eta}^I(t), \quad (3)$$

where intrinsic pseudo-chargeability, $\tilde{\eta}^I(t)$ is

$$\tilde{\eta}^I(t) = \frac{\eta}{(1 - \eta)\tau} e^{-\frac{t}{(1 - \eta)\tau}} u(t) \quad (4)$$

and $u(t)$ is Heaviside step function. This explicit expression for time domain Cole-Cole model can give us some insights about IP effect in time domain. Cole-Cole model in time domain is also shown in Figure 1. Used Cole-Cole parameters here are same as the above.

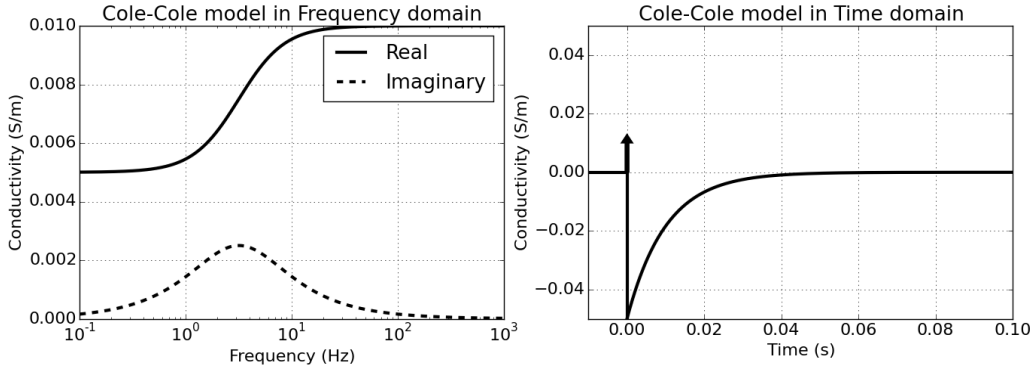


Figure 1: Cole-Cole model in frequency domain (a) and time (b) domain.

2.2 Convolution approach

Consider Maxwell's equations in time domain:

$$\vec{\nabla} \times \vec{e} = -\frac{\partial \vec{b}}{\partial t} \quad (5)$$

$$\vec{\nabla} \times \frac{1}{\mu} \vec{b} - \vec{j} = \vec{j}_s, \quad (6)$$

where \vec{e} is the electric field (V/m), \vec{b} is the magnetic flux density (Wb/m^2) and μ is the magnetic permeability (H/m). Here \vec{j} is the conduction current. In the frequency domain the current density \vec{J} is related to conductivity via $\vec{J}(\omega) = \sigma(\omega) \vec{E}(\omega)$ where \vec{E} is the electric field. Substituting equation (1) yields:

$$\vec{J}(\omega) = \sigma_\infty \vec{E}(\omega) + \vec{J}^{pol}(\omega), \quad (7)$$

where the polarization current ($\vec{J}^{pol}(\omega)$) is defined as

$$\vec{J}^{pol}(\omega) = \Delta\sigma(\omega) \vec{E}(\omega) \quad (8)$$

. Converting this relationship to time domain using a Fourier transform yields:

$$\vec{j}(t) = \sigma(t) \otimes \vec{e}(t), \quad (9)$$

where \otimes indicates time convolution. For causal signals, which is defined when $t \geq 0$, convolution between $a(t)$ and $b(t)$ can be written as

$$a(t) \otimes b(t) = \int_0^t a(u) b(t-u) du. \quad (10)$$

That is the current density depends upon the previous history of the electric field. Substituting equation (2) yields:

$$\vec{j}(t) = \sigma_\infty \vec{e}(t) + \Delta\sigma(t) \otimes \vec{e}(t) = \sigma_\infty \vec{e}(t) + \vec{j}^{pol}(t), \quad (11)$$

where $\vec{j}^{pol}(t) = \Delta\sigma(t) \otimes \vec{e}(t)$.

As an example, we consider a chargeable block that is subjected to a constant electric field, \vec{e}^{ss} (Figure 2). The superscript ss stands for steady-state. We assume the electric field does not change due to a chargeable body thus, $\vec{e}(t) = \vec{e}^{ss} u(t)$. Following [9], the first term in equation (11) can be considered as the current density if there were no polarization effects: fundamental current, $\vec{j}^F(t) = \sigma_\infty \vec{e}^{ss} u(t)$. By using Cole-Cole model with $c = 1$ and evaluating convolution in the polarization current density, we obtain

$$\vec{j}^{pol}(t) = -\eta \sigma_\infty [1 - e^{-\frac{t}{(1-\eta)\tau}}] \vec{e}^{ss} = -\tilde{\eta}(t) \sigma_\infty \vec{e}^{ss} \quad (12)$$

with the final value at $t = \infty$ yielding $\vec{j}^{pol} = -\eta \sigma_\infty \vec{e}^{ss} = -\eta \vec{j}^{ss}$ thus, $\eta = -\frac{\vec{j}^{pol}}{\vec{j}^{ss}}$, where $\vec{j}^{ss} = \sigma_\infty \vec{e}^{ss}$. That is, the chargeability can be considered as a fraction of the fundamental and steady-state current at the infinite time when the system reaches to the steady-state for the polarization charge build up. However on the other times, this fraction changes in time. In general case, we have the total current:

$$\vec{j}(t) = \vec{j}^F(t) + \vec{j}^{pol}(t) = (1 - \tilde{\eta}(t)) \vec{j}^{ss}, \quad (13)$$

where the pseudo-chargeability ($\tilde{\eta}$) is defined as

$$\tilde{\eta}(t) = -\frac{\vec{j}^{pol}}{\vec{j}^{ss}} \quad (14)$$

The pseudo-chargeability changes in time and end its values at $t = 0$ and ∞ are 0 and η , respectively. Here $\sigma_0 = (1 - \eta)\sigma_\infty$ indicates conductivity at zero frequency. Figure 3 shows the convolution between $\sigma(t)$ and $\vec{e}(t)$. Due to the polarization currents, the total current decreases after the switch on, and it reaches to the steady state at certain late time. The reason why the total current decrease is because the minus values in time dependent conductivity ($\sigma(t)$) when $t > 0$ as shown in Figure 1b.

Based on this analysis, we can obtain some insights about the conventional linearization in electrical field IP (EIP) and magnetic field IP (MIP) cases ([7, 8]), which uses both ends of complex conductivity in frequency domain: σ_0 and σ_∞ . We can define an effective conductivity as

$$\sigma_{eff}(t) = \frac{\vec{j}(t)}{\vec{e}^{ss}} = \sigma_\infty(1 - \tilde{\eta}(t)) = \sigma_\infty + \delta\sigma(t). \quad (15)$$

For $t \rightarrow \infty$, $\tilde{\eta} \rightarrow \eta$ (the intrinsic chargeability) and $\sigma_{eff} = \sigma_0 = \sigma_\infty(1 - \eta)$, which is well used result. Conversely, based on equation (15), we define an perturbed conductivity as

$$\delta\sigma(t) = -\sigma_\infty\tilde{\eta}(t) = \frac{\Delta\sigma(t) \otimes \vec{e}(t)}{\vec{e}^{ss}}. \quad (16)$$

Then we can rewrite equation (13) as

$$\vec{j}(t) = (\sigma_\infty + \delta\sigma(t))\vec{e}(t). \quad (17)$$

This is a principal statement of the linearization in time domain EIP and MIP responses, since it allows us to expand Maxwell's operator in terms of $\delta\sigma(t)$ for each time channel. Although the assumption about constant electric field allows us to have some insights about the polarization due to a chargeable body; however, it is not directly applicable to the general cases where the electric field changes due to not only the chargeable body, but also the conductive or resistive body. Therefore, this assumption should be released, and this will be treated later.

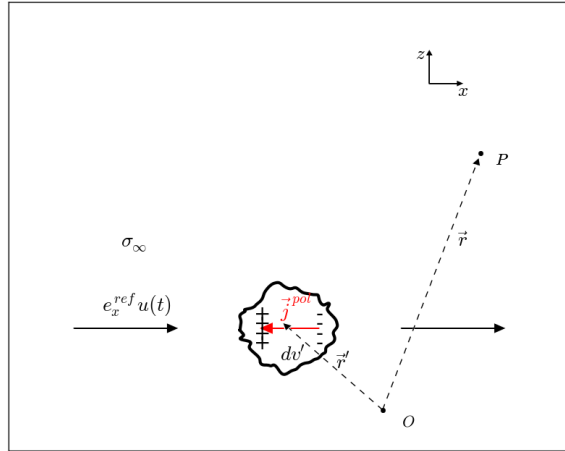


Figure 2: A chargeable block with the complex conductivity, which is subjected to a constant electric field, \bar{e}^{ss} .

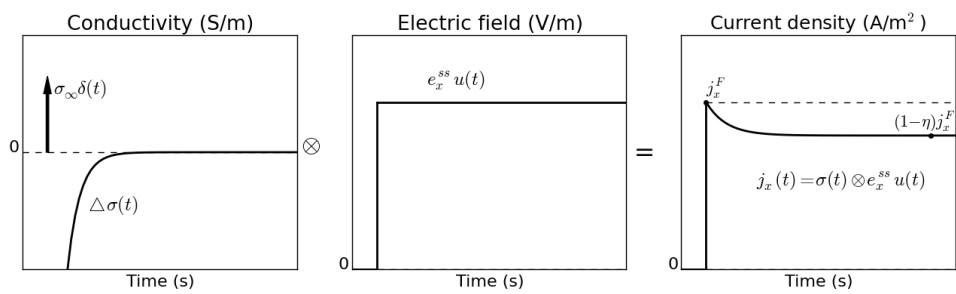


Figure 3: Convolution of time dependent conductivity ($\sigma(t)$) and step-on electric field in x -direction (e_x^{ss}).

2.3 Decomposition of EM responses

The basic ideas and notation presented thus far form the foundation of more general cases for grounded and airborne IP measurements. The difference arises because diffusion of the fields into the subsurface need to be taken into account and also electric fields due to the polarization can become important. As in [9], we let total fields as $\vec{e} = \vec{e}^F + \vec{e}^{IP}$, $\vec{b} = \vec{b}^F + \vec{b}^{IP}$ and $\vec{j} = \vec{j}^F + \vec{j}^{IP}$, where superscript F indicates fundamental and IP is induced polarization. Substituting into equations (5) and (6) yields the following sequences:

$$\vec{\nabla} \times (\vec{e}^F + \vec{e}^{IP}) = -\frac{\partial}{\partial t}(\vec{b}^F + \vec{b}^{IP}), \quad (18)$$

$$\vec{\nabla} \times \frac{1}{\mu}(\vec{b}^F + \vec{b}^{IP}) - (\vec{j}^F + \vec{j}^{IP}) = \vec{j}_s. \quad (19)$$

By canceling out vectors associated with EM terms, we have

$$\vec{\nabla} \times \vec{e}^{IP} = -\frac{\partial \vec{b}^{IP}}{\partial t}, \quad (20)$$

$$\vec{\nabla} \times \frac{1}{\mu} \vec{b}^{IP} = \vec{j}^{IP}. \quad (21)$$

In addition, associated EM equations can be written as

$$\vec{\nabla} \times \vec{e}^F = -\frac{\partial \vec{b}^F}{\partial t}, \quad (22)$$

$$\vec{\nabla} \times \frac{1}{\mu} \vec{b}^F - \vec{j}^F = \vec{j}_s. \quad (23)$$

Here

$$\vec{j}^F = \sigma_\infty \vec{e}^F, \quad (24)$$

$$\vec{j}^{IP} = \sigma_\infty \vec{e}^{IP} + \vec{j}^{pol}. \quad (25)$$

Note that the IP current density, \vec{j}^{IP} is the summation of the polarization current and $\sigma_\infty \vec{e}^{IP}$. Previously in convolution approach, we did not have this term because we assumed constant electric field ($\vec{e}(t) = \vec{e}^{ss}u(t)$). However, in general case, we need to consider this extra term due to polarization charge build up in the electric field.

Let $F[\cdot]$ denote operator associated with Maxwell's equations and let d denote the observed electromagnetic field thus, this includes both EM and IP effects. Keeping the same notation, we also write $d = d^F + d^{IP}$. Therefore, we define IP datum as

$$d^{IP} = d - d^F = F[\sigma_\infty \delta(t) + \Delta \sigma(t)] - F[\sigma_\infty \delta(t)]. \quad (26)$$

This subtraction process acts as an EM decoupling process, which reduces the EM effects in the measured responses. This formed the basics of work by [6]. Thus, assuming that we have a reasonable estimation for the distribution of σ_∞ in 3D space, we can identify IP datum, which are embedded in the observed responses.

Questions 1: Is it true that we have only IP effect with this subtraction process?

Doug: We need to show under what circumstances this is true. It is tied in with the statement that $\vec{\nabla} \times \vec{e}^{IP} = 0$. i.e. the polarization decays do not cause EM induction. Handling this matter here simplified much of the following paper.

Answer: I think that EM induction due to polarization decays are also IP effect, which is due to time dependent conductivity.

2.4 Thoughts on IP and polarization currents

With consideration of time dependent conductivity, current density was written as

$$\vec{j}(t) = \sigma_\infty \vec{e}(t) + \vec{j}^{pol}(t),$$

where $\vec{j}^{pol}(t) = \Delta\sigma(t) \otimes \vec{e}(t)$. Or this can be rewritten as

$$\vec{j}(t) = \vec{j}^F(t) + \vec{j}^{IP}(t),$$

where $\vec{j}^F(t) = \sigma_\infty \vec{e}^F(t)$ and

$$\vec{j}^{IP}(t) = \sigma_\infty \vec{e}^{IP}(t) + \vec{j}^{pol}(t). \quad (27)$$

We first consider the polarization current (\vec{j}^{pol}). Using the integral equation form for equations (20 and 21), \vec{e}^{IP} and \vec{b}^{IP} can be expressed as

$$\vec{e}^{IP}(\vec{r}; t) = \int_{\Omega} \bar{\mathbf{G}}^E(\vec{r}, \vec{r}_s) \otimes \vec{j}^{pol}(\vec{r}_s; t) d\vec{r}_s, \quad (28)$$

$$\vec{b}^{IP}(\vec{r}; t) = \int_{\Omega} \bar{\mathbf{G}}^B(\vec{r}, \vec{r}_s) \otimes \vec{j}^{pol}(\vec{r}_s; t) d\vec{r}_s, \quad (29)$$

where $\bar{\mathbf{G}}^E$ and $\bar{\mathbf{G}}^B$ are electric and magnetic green's tensors. Here \vec{j}^{pol} can be considered as a source term. Assuming that we know the polarization current and the above green's tensors, we can compute \vec{e}^{IP} and \vec{b}^{IP} by evaluating those integrals. This emphasizes the importance of the polarization current for the IP responses. In convolution approach, \vec{j}^{pol} was defined as

$$\vec{j}^{pol}(t) = -\tilde{\eta}(t) \sigma_\infty \vec{e}^{ss} = -\tilde{\eta}(t) \vec{j}^{ref}, \quad (30)$$

where the reference current density is $\vec{j}^{ref} = \vec{j}^{ss} = \sigma_\infty \vec{e}^{ss}$. This allows to build up a conceptual model of the IP responses: an IP body acts like a dipole which has opposite direction to reference current density, and proportional to $\tilde{\eta}$. This conceptual model is analogous to Seigel's one ([7]).

Second, we treat IP current density \vec{j}^{IP} . Based on equation (21), we can apply Biot-Savart law:

$$\vec{b}^{IP}(\vec{r}; t) = \frac{\mu_0}{4\pi} \int_{\Omega} \frac{\vec{j}^{IP}(\vec{r}_s; t) \times \hat{r}}{|\vec{r} - \vec{r}_s|^2} d\vec{r}_s. \quad (31)$$

This equation shows that we can compute \vec{b}^{IP} using \vec{j}^{IP} . Different from the magnetic greens tensor ($\bar{\mathbf{G}}^B$), a kernel in Biot-Savart law is purely geometric. However we need to know the additional term $\sigma_\infty \vec{e}^{IP}$ to compute \vec{b}^{IP} using Biot-Savart law. This is caused by difference between $\bar{\mathbf{G}}^B$ and kernel function of Biot-Savart law. Both approaches can be useful in spite of some different features. These two kernels can be same for a specific case where we do not have any conductivity contrast in σ_∞ without any EM induction effect. Biot-savart law can have different form (CITE):

$$\vec{b}^{IP}(\vec{r}; t) = \frac{\mu_0}{4\pi} \int_{\Omega} \frac{\vec{\nabla}_s \times \vec{j}^{IP}(\vec{r}_s; t)}{|\vec{r} - \vec{r}_s|} d\vec{r}_s. \quad (32)$$

If we let $\vec{e}^{IP} = -\vec{\nabla} \phi^{IP}$ and σ_∞ is constant, then we can substitute \vec{j}^{IP} in above equation as \vec{j}^{pol} because $\vec{\nabla} \times \vec{\nabla} \phi^{IP} = 0$. This result shows that we do not need to know $\sigma_\infty \vec{e}^{IP}$ term to compute \vec{b}^{IP} for this specific case.

We have recognized that \vec{j}^{IP} can be a fundamental element of understanding IP responses. In order to get some insights of \vec{j}^{IP} , we decompose \vec{j}^{IP} as

$$\vec{j}^{IP}(t) = \sigma_\infty \vec{e}^{IP}(t) + \Delta\sigma(t) \otimes \vec{e}^F(t) + \Delta\sigma(t) \otimes \vec{e}^{IP}(t). \quad (33)$$

For notational convenience, we respectively refer to $\sigma_\infty \vec{e}^{IP}(t)$, $\Delta\sigma(t) \otimes \vec{e}^F(t)$ and $\Delta\sigma(t) \otimes \vec{e}^{IP}(t)$ as \vec{j}_1^{IP} , \vec{j}_2^{IP} and \vec{j}_3^{IP} . Characteristics of each current density are following. We start with \vec{j}_1^{IP} . This is defined everywhere. This is the term makes a difference between \vec{j}^{IP} and \vec{j}^{pol} . Recalling Smiths approximate convolution approach ([9]), he assumed \vec{j}_1^{IP} and \vec{j}_3^{IP} are negligible, which makes $\vec{j}^{IP} = \vec{j}^{pol}$. In his case, an IP body was surrounded by the free space and $\eta \ll 1$. However, in general case where the background medium is not free space, this term may not be negligible in that \vec{j}_2^{IP} and \vec{j}_3^{IP} are only defined in the IP body because $\Delta\sigma(t)$ is zero except for the IP body. This shows that \vec{j}_2^{IP} is going to be the main term of \vec{j}^{IP} in the IP body as the conductivity of background medium and η decrease. In addition, \vec{j}_3^{IP} might be negligible when we have small η . However, it is hard to suggest that when we have considerable η , since this is convoluted property of \vec{e}^{IP} and $\Delta\sigma(t)$.

3 Linearization of IP responses

3.1 Linearization in EIP and MIP

For the linearization of IP response, it is useful to think in terms of EIP or MIP experiment where we apply a direct current into the ground. We use step-on waveform. Neglecting induction, $F[\sigma_\infty] = F_{DC}[\sigma_\infty] \rightarrow \vec{e}_{\sigma_\infty}^{ss}$, where $F_{DC}[\cdot]$ indicates steady-state Maxwell's operator. Recalling the definitions of $\delta\sigma$ and σ_{eff} that we have made in convolution approach, we approximately rewrite total current density, \vec{j} as

$$\vec{j}(t) \approx (\sigma_\infty + \delta\sigma(t))\vec{e}(t) = \sigma_{eff}(t)\vec{e}(t). \quad (34)$$

The perturbed conductivity and effective conductivity were defined as $\delta\sigma = \frac{\Delta\sigma(t) \otimes \vec{e}(t)}{\vec{e}^{ss}}$ and $\sigma_{eff} = \frac{\vec{j}}{\vec{e}^{ss}}$. Considering that we use step-on waveform, this is reasonable approximation, since $\vec{e}(t) \approx \vec{e}^{ss}u(t)$ when $\eta \ll 1$. By substituting \vec{e}^{ss} in $\delta\sigma(t)$ with $\vec{e}(t)$, equation (34) can be converted to an equality equation. By substituting the constant electric field \vec{e}^{ss} as $\vec{e}_{\sigma_\infty}^{ss}$, we let

$$\Delta\sigma(t) \otimes \vec{e}(t) = \vec{j}^{pol}(t) \approx \delta\sigma(t)\vec{e}(t). \quad (35)$$

Based on this assumption for EIP problem, IP response at any time $t > 0$ can be expressed as $F_{DC}[\sigma_{eff}(t)]$. Then we make Taylor expansion and obtain

$$F_{DC}[\sigma_\infty + \delta\sigma_i] = F_{DC}[\sigma_\infty] + \frac{\partial F_{DC}[\sigma_\infty]}{\partial \sigma_\infty} \delta\sigma_i + O(\delta\sigma_i^2), \quad (36)$$

where subscript i indicates i^{th} time channel. By ignoring the second order term in equation (36) with some linear algebra, we obtain the IP datum at i^{th} time channel:

$$d_i^{IP} = F_{DC}[\sigma_\infty + \delta\sigma_i] - F_{DC}[\sigma_\infty] \approx -\frac{\partial F_{DC}[\sigma_\infty]}{\partial \log(\sigma_\infty)} \tilde{\eta}_i, \quad (37)$$

where $\tilde{\eta}_i = -\frac{\delta\sigma_i}{\sigma_\infty}$. This constructs a general formulation of linear inverse problem in EIP ([10], [3]). In addition, this still applicable to MIP case ([8], [1]).

Conversely, all of our derivations has been done for a step-on current. Then what happen if the data are measured in the off-time? Off time response (d_{off}^{IP}) can be simply computed using on-time response (d_{on}^{IP}), using the following relationship:

$$d_{off}^{IP}(t) = d_{on}^{IP}(t = \infty) - d_{on}^{IP}(t) = F_{DC}[\sigma_0] - d_{on}^{IP}(t), \quad (38)$$

where $\sigma_0 = \sigma_\infty(1 - \eta)$, which is the low frequency limit of Cole-Cole model. This indicates that we can still use equation (37), because the off-time result is directly related to the on-time as illustrated in Figure 4. However, in practice, the input current waveform can be arbitrary as shown in Figure 5. We let a current waveform as $I_0 w(t)$, where I_0 is the magnitude of the current and $w(t)$ is that of the time dependency. The maximum charging will occur when a uniform field has been applied for a duration $t \gg \tau$. Let \vec{e}^{ss} represents the steady state field associated with $I(t) = I_0 u(t)$. In this case, the assumption that we made for \vec{j}^{pol} (equation (35)) may not be reasonable, because the total electric field, $\vec{e}(t)$ can dynamically change due to $w(t)$ so that the electric field at i^{th} time channel, \vec{e}_i can be quite different from \vec{e}^{ss} as shown in Figure 5. Therefore, for this general waveform, it is not straight forward to linearize EIP responses with the current framework.

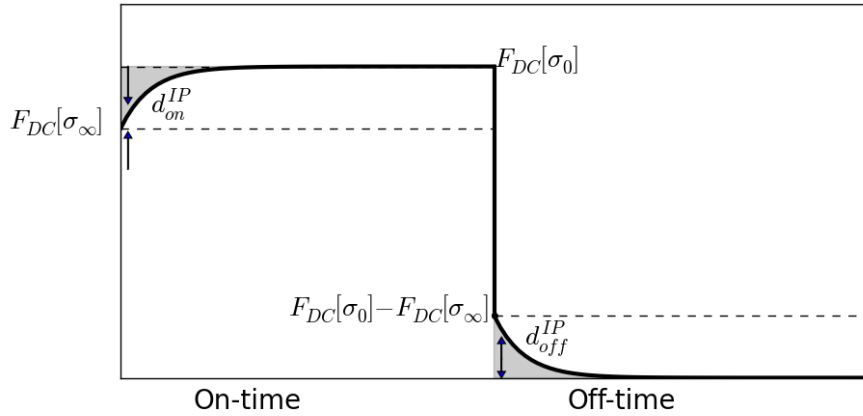


Figure 4: Time domain EIP curve.

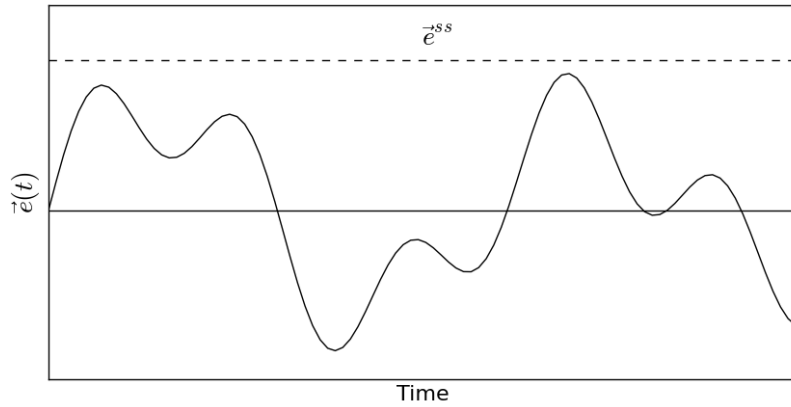


Figure 5: Conceptual diagram of oscillating electric field.

3.2 Linearization in TEM-IP

In previous two sections, we have treated the linearization of the IP responses without consideration of the EM induction effect. The fundamental responses of EIP and Mip cases with step-on or step-off waveform were independent on time thus, any time dependent responses are due to the IP effect. However, ignoring EM induction effect may not be reasonable, in particular, inductive source TEM case can be a representative example because the EM induction is the driving force of the system. Therefore, we need to release this assumption to handle those situations where we cannot ignore EM induction effect. Now a principal difference from the steady-state IP case is not only the IP-related fields, but also the fundamental fields can be time dependent. However, we still want to use a similar linearization approach from the steady-state case, which expands Maxwell's operator in terms of $\delta\sigma(t)$. A significant problem here is the EM induction term $(\frac{\partial\vec{b}}{\partial t})$ in equation (5). This term makes a coupling between the current and previous time channels, thus expanding this operator in terms of $\delta\sigma(t)$:

$$F[\sigma_\infty + \Delta\sigma(t)] \approx F[\sigma_\infty] + \frac{\partial F[\sigma_\infty]}{\partial \sigma_\infty} \delta\sigma$$

is not valid. Accordingly, we need a different approach to tackle this problem, although most of the principal methodologies used in the EIP and MIP case can be similarly applied.

Nonetheless, our goal is still similar as before: we want to express d^{IP} as a function of the pseudo-chargeability ($\tilde{\eta}(t)$) in time. Therefore, we can have a form of linear equation like $d^{IP}(t) = -J[\tilde{\eta}(t)]$, where $J[\cdot]$ is a linear operator, which is independent on time. For this, we consider a general system whether we can consider either grounded or inductive source and any types of measured field. Let the total electric field, $\vec{e}(t)$ can be approximated as

$$\vec{e}(t) \approx \vec{e}^{ref} w^e(t), \quad (39)$$

where $w^e(t)$ is defined as:

$$w^e(t) = \begin{cases} w^{ref}(t) & w^{ref}(t) \geq 0 \\ 0 & \text{if } w^{ref}(t) < 0, \end{cases} \quad (40)$$

with

$$w^{ref}(t) = \frac{\vec{e}(t) \cdot \vec{e}^{ref}}{\vec{e}^{ref} \cdot \vec{e}^{ref}}. \quad (41)$$

Here $w^{ref}(t)$ is a dimensionless function that prescribes the time history of the electric field at each location and the reference electric field (\vec{e}^{ref}) is an appropriate scaling for the electric field, which is independent on time. This indicates that the direction of the electric field does not change in time. In addition, by the definition of $w^e(t)$, we project negative values of $w^{ref}(t)$ to zero. Note that this assumption is only applied to the second term on right-hand side of equation (25). Substituting this into equation (25) yields

$$\vec{j}^{IP}(t) \approx \sigma_\infty \vec{e}^{IP}(t) + \frac{\Delta\sigma(t) \otimes w^e(t)}{\sigma_\infty} \vec{j}^{ref},$$

where the reference current density is defined as

$$\vec{j}^{ref} = \sigma_\infty \vec{e}^{ref}. \quad (42)$$

Letting pseudo-chargeability as

$$\tilde{\eta}(t) = -\frac{\Delta\sigma(t) \otimes w^e(t)}{\sigma_\infty} \approx -\frac{\vec{j}^{pol}}{\vec{j}^{ref}}, \quad (43)$$

we obtain

$$\vec{j}^{IP}(t) = \sigma_\infty \vec{e}^{IP}(t) + \vec{j}^{pol}(t) \approx \sigma_\infty \vec{e}^{IP}(t) - \vec{j}^{ref} \tilde{\eta}(t). \quad (44)$$

A physical insight about the pseudo-chargeability is that a fraction of polarization current and reference current. Because the reference current is time-independent property, any time-dependency in the pseudo-chargeability is from the polarization current. Using Helmholtz decomposition, \vec{e} can be decomposed as $\vec{e} = -\vec{a} - \vec{\nabla}\phi$, where \vec{a} and ϕ is electric vector and scalar potentials, respectively and $\nabla \cdot \vec{a} = 0$. Physically, those two terms indicate charge-build up and EM induction effects, which induce galvanic and vortex currents, respectively. So, \vec{e}^{IP} can be decomposed as

$$\vec{e}^{IP} = -\vec{a}^{IP} - \vec{\nabla}\phi^{IP}. \quad (45)$$

Now we make an another assumption:

$$\vec{e}^{IP} \approx \vec{e}_{approx}^{IP} = -\vec{\nabla}\phi^{IP}, \quad (46)$$

which means \vec{e}^{IP} term in equation (44) is dominated by galvanic effect ($\frac{\partial \vec{b}^{IP}}{\partial t} \approx 0$). First taking $\nabla \cdot$ to equation (44) then by substituting \vec{e}^{IP} with equation (46) with some linear algebra, we obtain

$$\phi^{IP}(t) \approx -[\nabla \cdot \sigma_\infty \vec{\nabla}]^{-1} \nabla \cdot \vec{j}^{ref} \tilde{\eta}(t). \quad (47)$$

By taking $\vec{\nabla}$ to this equation we have

$$\vec{e}_{approx}^{IP} = \vec{\nabla}[\nabla \cdot \sigma_\infty \vec{\nabla}]^{-1} \nabla \cdot \vec{j}^{ref} \tilde{\eta}(t). \quad (48)$$

Thus, the electric field due to the IP effect can be expressed as a function of $\tilde{\eta}(t)$ in time.

The observd data can be \vec{b} or $\frac{\partial \vec{b}}{\partial t}$ in some cases thus, we need to compute \vec{b}^{IP} or $\frac{\partial \vec{b}^{IP}}{\partial t}$. For this, we first compute \vec{j}^{IP} then use Biot-Savart law to compute \vec{b}^{IP} or $\frac{\partial \vec{b}^{IP}}{\partial t}$. Substituting equation (47) into equation (44), approximated IP current density, \vec{j}_{approx}^{IP} can be expressed as

$$\vec{j}^{IP}(t) \approx \vec{j}_{approx}^{IP} = -\bar{S}\sigma_\infty \vec{e}^{ref} \tilde{\eta}(t), \quad (49)$$

where

$$\bar{S} = -\sigma_\infty \vec{\nabla}[\nabla \cdot \sigma_\infty \vec{\nabla}]^{-1} \nabla \cdot + \bar{I} \quad (50)$$

and \bar{I} is an identity tensor. Then by using Biot-Savart law we have:

$$\vec{b}_{approx}^{IP}(\vec{r}; t) = -\frac{\mu_0}{4\pi} \int_{\Omega} \frac{\bar{S}\vec{e}^{ref}(\vec{r}_s) \times \hat{r}}{|\vec{r} - \vec{r}_s|^2} \tilde{\eta}(t) d\vec{r}_s. \quad (51)$$

By taking time derivative to the above equation we have

$$\frac{\partial \vec{b}_{approx}^{IP}}{\partial t}(\vec{r}) = -\frac{\mu_0}{4\pi} \int_{\Omega} \frac{\bar{S}\vec{e}^{ref}(\vec{r}_s) \times \hat{r}}{|\vec{r} - \vec{r}_s|^2} \frac{\partial}{\partial t} \tilde{\eta}(t) d\vec{r}_s. \quad (52)$$

Both equations (51) and (52) are function of $\tilde{\eta}(t)$, and the time dependency only rises from $\tilde{\eta}(t)$. To summarize, with the assumption that \vec{e}^{IP} is mostly galvanic, we show that electromagnetic fields due to IP effects can be expressed as instantaneous property, which have linear relationship with $\tilde{\eta}(t)$. Therefore, d^{IP} responses, which can be any type of electromagnetic fields, can be represented as $d^{IP}(t) = -J[\tilde{\eta}(t)]$. In discretized space this can be expressed as

$$\mathbf{d}_i^{IP} = -\mathbf{J}\tilde{\eta}_i, \quad (53)$$

where \mathbf{J} is corresponding sensitivity matrix and the subscript i indicates i^{th} time channel. Boldface of upper and lower cases indicate a matrix and column vector in discretized space. Since d^{IP} can be any types of electromagnetic fields, our approach to linearize time domain IP responses is applicable for any types of TEM surveys, whereas some details for practical application might be somewhat different. However, the fundamental concept will be same.

On the other hand, we must carefully investigate the assumptions that we have made to formulate this linear relationship, and a fundamental characteristics of what we are recovering; thus, we need to identify four fundamental points. We made two assumptions: (a) we know exact background conductivity model (σ_∞). (b) Inductive effect in \vec{e}^{IP} is negligible. (c) $\Delta\sigma(t) \otimes \vec{e}(t) = -\tilde{\eta}(t)\vec{j}^{ref}$, In addition, (d) we recognized that $\tilde{\eta}(t)$ is convoluted property with $\vec{e}(t)$ and distributed IP parameters. Those four points are not trivial to be validated in physical or mathematical ways; thus each of them should be carefully tested with numerical experiments for different types TEM surveys like grounded or inductive source TEM methods and different conductivity structures.

3.3 Discussions

3.3.1 Choice of reference electric field

We first consider the choice of the reference electric field for the grounded source IP case. Although we have the EM induction effect for the grounded source case, here we assume the EM induction effect is minor to the galvanic effect. Thus, the time behaviour of the fundamental electric field with step-on and -off waveform will be same as that of the input current as shown in Figure 6a. The choice of the reference electric field in this case is intuitive, because the fundamental electric field is constant on on-time period. That is, we choose the electric field at the steady-state with σ_∞ ($\vec{e}_{\sigma_\infty}^{ss}$) as \vec{e}^{ref} . This will be a reasonable choice for the grounded source case even if we consider EM induction effect.

A fundamental difference from galvanic and inductive source arises from the property, $\nabla \cdot \vec{j}_s$. If this is zero then it is inductive source or if not, it is galvanic source. In order to get some insight, consider DC problem for inductive source:

$$\begin{aligned} -\nabla \cdot \vec{j}^{ss} &= \nabla \cdot \vec{j}_s = 0, \\ \nabla \cdot \sigma_\infty \vec{\nabla} \phi_{\sigma_\infty}^{ss} &= -\nabla \cdot \vec{j}_s = 0. \end{aligned}$$

Since the right-hand side of the above equation is zero, thus, $\phi_{\sigma_\infty}^{ss} = 0$ and $\vec{e}_{\sigma_\infty}^{ss} = 0$. This shows that there are no DC fields for inductive source case.

For the inductive source case, we cannot ignore the EM induction effect because it is the driving force of the system. We consider the magnitude of the electric field at a single pixel in the earth with a step-off waveform. As shown in Figure 6b, this will start from zero, reaches to the maximum then decays. We choose the fundamental electric field at the maximum as the reference electric field. Mathematical representation of this choice can be written as

$$\vec{e}^{ref} = \vec{e}_{max}^F = \vec{e}^F(t) \otimes \delta(t - t^{max}), \quad (54)$$

where t^{max} is the time when the magnitude of the fundamental electric fields reach to the maximum. Note that t_{max} is variable in 3D space, since the electric field at each pixel in 3D space can have different time decaying feature due to the source location and conductivity distribution. The reason why we define the reference electric field is due to the approximation for the polarization currents: $\vec{j}^{pol} = -\vec{j}^{ref}\tilde{\eta}$, where $\vec{j}^{ref} = \sigma_\infty \vec{e}^{ref}$. An important reasoning behind this approximation is that the amplitude of the polarization current is proportional to the reference current, and that of the direction does not change dramatically in time. Therefore,

choosing the fundamental electric field at the time when it reaches to the maximum indicates that the amplitude of the polarization current is proportional to the reference current at this time, and the direction of the polarization current is similar to that of the reference current. This explanation is applicable for both galvanic and inductive source IP cases. The reference electric field for the galvanic source cases can be the fundamental electric field at the maximum as well (\dot{e}_max^F).

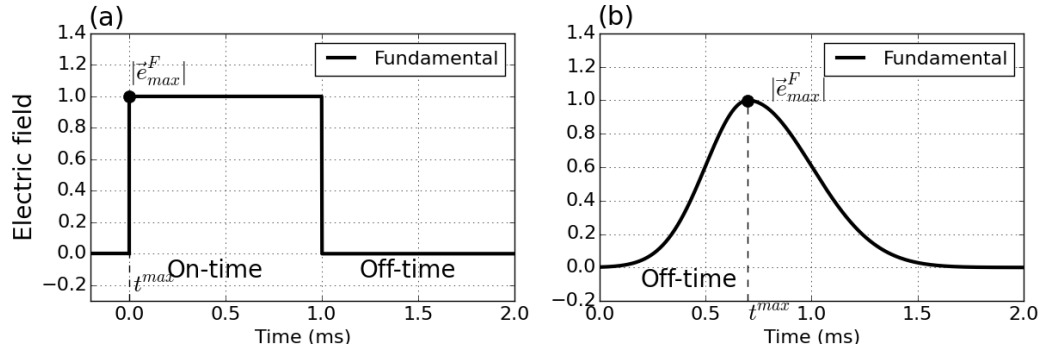


Figure 6: Conceptual diagram for the amplitude of the fundamental electric fields. (a) Galvanic and (b) inductive source IP cases.

Constant ramp for the inductive source: obtain same analogy for grounded source case (constant electric field)

Polarization charge build up reaches to the steady state

3.3.2 Revisitation of EIP and MIP

In previous section, we suggested a linearization methodology, which can be applied to general TEM problems. Using this methodology, we revisit the linearization of the IP responses in EIP and MIP cases. Recall that we had a challenge in linearization when we have general current waveform.

As we mentioned on previous section, a proper reference electric field for EIP and MIP cases can be $\vec{e}_{\sigma_\infty}^{ss}$, so we modify equation (39) as

$$\vec{e}(t) \approx \vec{e}_{\sigma_\infty}^{ss} w^e(t).$$

Then $\phi^{IP}(t)$ shown in equation (47), can be rewritten as

$$\begin{aligned} \phi^{IP}(t) \approx \phi_{approx}^{IP} &= -[\nabla \cdot \sigma_\infty \vec{\nabla}]^{-1} \nabla \cdot \vec{\nabla} \phi_{\sigma_\infty}^{ss} (\Delta\sigma(t) \otimes w^e(t)) \\ &= \frac{\partial \phi_{\sigma_\infty}^{ss}}{\partial \sigma_\infty} \Delta\sigma(t) \otimes w^e(t) \end{aligned}$$

and finally we have

$$\begin{aligned} \phi_{approx}^{IP}(t) &= \frac{\partial \phi_{\sigma_\infty}^{ss}}{\partial \sigma_\infty} \Delta\sigma(t) \otimes w^e(t) \\ &= \frac{\partial \phi_{\sigma_\infty}^{ss}}{\partial \sigma_\infty} \delta\sigma(t) \end{aligned} \quad (55)$$

where $\delta\sigma(t) = \frac{\Delta\sigma(t) \otimes \vec{e}(t)}{\vec{e}_{\sigma_\infty}^{ss}} = \Delta\sigma(t) \otimes w^e(t)$ and

$$\frac{\partial \phi_{\sigma_\infty}^{ss}}{\partial \sigma_\infty} = -[\nabla \cdot \sigma_\infty \vec{\nabla}]^{-1} \nabla \cdot \vec{\nabla} \phi_{\sigma_\infty}^{ss}. \quad (56)$$

Detailed derivation of equation (56) in discretized space is given in appendix ???. Substituting equation (43) to (56), we have

$$\phi_{approx}^{IP}(t) = -\frac{\partial \phi_{\sigma_\infty}^{ss}}{\partial \log(\sigma_\infty)} \tilde{\eta}(t), \quad (57)$$

which is the same result from equation (37) for electrical potential. Therefore, we can derive same result with conventional linearization in EIP case using suggested methodology. \vec{e}^{IP} can also be linearized in the same way, since we can just take gradient to the above equation and obtain \vec{e}^{IP} .

For MIP case, we measure the magnetic flux density, and we linearized \vec{b}^{IP} by expanding Maxwell's operator. However, in this time we use the suggested linearization approach for the general case. Modifying equation (44), we obtain

$$\begin{aligned} \vec{j}^{IP}(t) &= \sigma_\infty \vec{e}^{IP}(t) + \Delta\sigma(t) \otimes w^e(t) \vec{e}_{\sigma_\infty}^{ss} \\ &= -\bar{S} \sigma_\infty \vec{e}_{\sigma_\infty}^{ss} \tilde{\eta}(t). \end{aligned} \quad (58)$$

Applying Biot-Savart law yields

$$\vec{b}^{IP}(\vec{r}; t) = -\frac{\mu_0}{4\pi} \int_{\Omega} \frac{\bar{S} \vec{e}_{\sigma_\infty}^{ss}(\vec{r}_s) \times \hat{r}}{|\vec{r} - \vec{r}_s|^2} \tilde{\eta}(t) d\vec{r}_s. \quad (59)$$

Different from conventional linearization approach used in EIP and MIP cases, applicability of our linearization method is not limited to step-on or step-off waveform, but general. Therefore, even when we have general waveform, which can be oscillating as shown in Figure 5, the linearization of EIP or MIP can still proceed. Furthermore, considering an oscillating input current as shown in Figure 5 also supports this statement, because $|\delta(t)| \ll \sigma_\infty \eta$.

3.3.3 Ignoring inductive IP effect

In controlled-source EM (CSEM) experiments, we can have two types of sources: grounded and inductive sources. We first consider this assumption for grounded source. Ignoring inductive part of IP effect $\frac{\partial \vec{b}^{IP}}{\partial t} \approx 0$, might be reasonable for grounded source case, since galvanic effect can be dominant ($\vec{\nabla} \phi^{IP} \gg \vec{a}^{IP}$) in most cases, but this should be carefully tested because it depends on the conductivity structure and time.

Different from the galvanic source, for the inductive source case, the EM induction is the main driving force of the system. Therefore, we need to be more careful when we ignore inductive IP effect. Consider a situation where we have homogeneous background conductivity model ($\sigma_\infty = \text{constant}$). Recall \vec{j}^{IP} with Helmholtz decomposition:

$$\begin{aligned}\vec{j}^{IP} &= \sigma_\infty \vec{e}^{IP} + \Delta\sigma(t) \otimes w^e(t) \vec{e}^{ref} \\ &= -\sigma_\infty (\vec{\nabla} \phi^{IP} + \vec{a}^{IP}) + \Delta\sigma(t) \otimes w^e(t) \vec{e}^{ref}\end{aligned}$$

By taking $\nabla \cdot$ we have

$$-\nabla \cdot \sigma_\infty \vec{\nabla} \phi^{IP} - \nabla \cdot \sigma_\infty \vec{a}^{IP} = -\nabla \cdot \Delta\sigma(t) \otimes w^e(t) \vec{e}^{ref}.$$

Since σ_∞ is constant in space, then we rewrite

$$\nabla \cdot \sigma_\infty \vec{\nabla} \phi^{IP} = \vec{j}_{approx}^{pol},$$

where $\nabla \cdot \vec{a}^{IP} = 0$ and $\vec{j}_{approx}^{pol} = \nabla \cdot \Delta\sigma(t) \otimes w^e(t) \vec{e}^{ref}$. Therefore, once we do not have any conductivity variation in our background conductivity model, we can obtain reasonable ϕ^{IP} by solving above system. This indicates we can compute IP responses, which are related to galvanic effect, while we still can have significant induction portion, \vec{a}^{IP} in \vec{e}^{IP} . Note that $\nabla \cdot \vec{a}^{IP} = 0$ does not mean $\vec{a}^{IP} = 0$. Further in general case where we have conductivity constraint in the earth, $\nabla \cdot \sigma_\infty \vec{a}^{IP}$ may not be zero, thus the relative strength of $\sigma_\infty \vec{a}^{IP}$ to \vec{j}_{approx}^{pol} should be minor to make our assumption reasonable. Intuitively, we know that EM induction effect is going to decay faster than galvanic effect so that they are going to small in late time channels. To account for this effect, we consider Faraday's law

$$\vec{\nabla} \times \vec{a}^{IP}(t) = \frac{\partial \vec{b}^{IP}(t)}{\partial t},$$

since $\vec{\nabla} \times \vec{\nabla} \phi^{IP} = 0$. This tells us time varying magnetic flux density generate rotational electric field, that is \vec{a}^{IP} . This induced IP effect may have an influence on polarization charge build up (ϕ^{IP}) due to the term $\nabla \cdot \sigma_\infty \vec{a}^{IP}$, when we have conductivity constraint in the earth. Relative influence of this term will vary for different conductivity structures. In frequency domain equation, we have

$$\vec{\nabla} \times \vec{A}^{IP}(\omega) = \omega \vec{B}^{IP}(\omega).$$

The magnitude of \vec{A}^{IP} is proportional to ω in frequency domain. As ω decrease, EM induction effect gets smaller. Accordingly, \vec{a}^{IP} in \vec{e}^{IP} gets smaller as we move on to late time channels, thus galvanic term ϕ^{IP} can be dominant term in \vec{e}^{IP} at certain late time channels. Those are possible situations that we are interested for IP signals and we might have some chances to apply our linearization methodology.

4 IP inversion methodology

4.1 IP inversion procedure

Considering practical point of view, the IP inversion of TEM data can have multiple steps including some processings and the application of the 3D inversion. Therefore, we suggest a procedure of the 3D IP inversion for TEM data as following.

To obtain the fundamental EM response, d^F , (a) invert TEM data and recover a 3D conductivity model (σ_{est}). This may involve omitting data that are obviously contaminated with IP signals, such as the existence of negative transients in coincident loop surveys. (b) Forward modelling then yields an approximate value of d^F and subtract it from the observations, d . However, we cannot get the correct d^F , since the estimated conductivity is not exact. (c) Therefore the computed d^{IP} data may have some errors containing both a residual field due to the incorrect conductivity ($\Delta d[\sigma_\infty](t)$) and some noises ($n(t)$). To examine these more closely we write

$$d_{obs}^{IP}(t) = d(t) - d[\sigma_{est}](t) = d^{IP}(t) + \Delta d[\sigma_\infty](t) + n(t), \quad (60)$$

where d_{obs}^{IP} is raw d^{IP} data, d^{IP} is the true IP data, n is additive noise, and $\Delta d[\sigma_\infty]$ ($= d^F - d[\sigma_{est}]$) is the error caused because of poor estimate of σ_∞ . We assume this residual field is a large-scale smoothly varying perturbation to the d^{IP} data and refer to it as regional field. A simple approach that we can possibly estimate this: fit the computed d_{obs}^{IP} data with a low order polynomial. Then subtract that from the d^{IP} data. This regional removal process can be expressed as

$$d_{obs}^{IP}(t) - \Delta d[\sigma_\infty](t) = d^{IP} + n(t) \quad (61)$$

(d) The final data are linearly related to a pseudo-chargeability through a sensitivity function shown in equation (53). (e) The d^{IP} at various time channels can be inverted individually. The pseudo-chargeability models may be useful in themselves or they may be further processed to estimate Cole-Cole, or equivalent parameters.

4.2 An equivalent pseudo-chargeability

We derived a linearized kernel function of d^{IP} response as a function of the pseudo-chargeability ($\tilde{\eta}(t)$) for various types of surveys including TEM, EIP and MIP. Note that the pseudo-chargeability is defined for each transmitter that is, they are different for each transmitter, because each transmitter will have different excitation of the earth. This indicates that IP response should be defined as

$$d_k^{IP}(t) = J_k[\tilde{\eta}_k(t)], \quad k = 1, \dots, nTx, \quad (62)$$

the subscript k indicates k -th sounding and nTx is the number of soundings. Reminding that our goal is the 3D IP inversion using this linearized kernel function, this induces a problem that we have nTx pseudo-chargeability distribution that we need to recover. Setting up an inverse problem in this cause extremely non-unique problem thus, we want to recover an equivalent pseudo-chargeability ($\tilde{\eta}_{eqv}$), which represents pseudo-chargeability from every sounding with reasonable explanation of the IP responses.

From the definition shown in equation (43), we recognize that the pseudo-chargeability is fraction of the polarization and the reference current. Using the normalization of the polarization current with the reference current, which will be different for each transmitter, we want to make pseudo-chargeability as an independent property for each transmitter. This will depend on $w^e(t)$, because the pseudo-chargeability is the convolution between $\tilde{\eta}^I(t)$ and $w^e(t)$:

$$\tilde{\eta}_k(t) = \tilde{\eta}^I(t) \otimes w_k^e(t), \quad (63)$$

Therefore, if w_k^e is same for all sounding locations, then we can let $\tilde{\eta}_{eqv} = \tilde{\eta}_k$, $k = 1, \dots, nTx$. Based on this we obtain a linear equation for IP responses as

$$d_i^{IP} = J[\tilde{\eta}_{eqv} \ i], \quad (64)$$

where the sensitivity function, $J[\cdot]$ takes $\tilde{\eta}_{eqv} \ i$, and outputs d_i^{IP} responses for all soundings at the i -th time. Availability of the equivalent pseudo-chargeability may different from different types of surveys and conductivity structures thus, it should be carefully investigated.

4.3 3D IP inversion with linearized kernel

To set up an linear inverse problem we rewrite equation (53) as

$$\mathbf{d}^{pred} = \mathbf{A}\mathbf{m}, \quad (65)$$

where \mathbf{A} is sensitivity matrix of linear problem, which corresponds to \mathbf{J} shown in equation (53), \mathbf{d}^{pred} is IP responses at k^{th} time channel (\mathbf{d}_k^{IP}), \mathbf{m} is distributed model parameters, which can be either $\tilde{\eta}_k$ or $\frac{\partial}{\partial t} \tilde{\eta}_k$. This presents that we invert each time channel of d^{IP} , separately. Our inversion methodology is based upon that described in [5]. The solution to the inverse problem is the model \mathbf{m} that solves the optimization problem

$$\begin{aligned} & \text{minimize } \phi = \phi_d(\mathbf{m}) + \phi_m(\mathbf{m}) \\ & \text{s.t. } 0 \leq \mathbf{m}, \end{aligned} \quad (66)$$

where ϕ_d is a measure of data misfit, ϕ_m is a user defined model objective function and β is regularization or trade-off parameter. We use the sum of the squares to measure data misfit

$$\phi_d = \|\mathbf{W}_d(\mathbf{A}\mathbf{m} - \mathbf{d})\|_2^2 = \sum_{j=1}^N \left(\frac{\mathbf{d}_j^{pred} - \mathbf{d}_j^{obs}}{\epsilon_j} \right)^2, \quad (67)$$

where N is the number of the observed data and \mathbf{W}_d is a diagonal data weighting matrix which contains the reciprocal of the esitmated uncertainty of each datum (ϵ_j) on the main diagonal, \mathbf{d}^{obs} is a vector containing the observed data, \mathbf{d}^{pred} is a vector containing calculated data from a linear equation given in equation (65). The model objective function, ϕ_m is a measure of amount structure in the model and, upon minimization, will generate a smooth model which is close to a reference model, \mathbf{m}_{ref} . We define ϕ_m as

$$\begin{aligned} \phi_m = & \alpha_s \|\mathbf{W}_s \mathbf{W}(\mathbf{m} - \mathbf{m}_{ref})\|_2^2 + \alpha_x \|\mathbf{W}_x \mathbf{W}(\mathbf{m} - \mathbf{m}_{ref})\|_2^2 + \\ & \alpha_y \|\mathbf{W}_y \mathbf{W}(\mathbf{m} - \mathbf{m}_{ref})\|_2^2 + \alpha_z \|\mathbf{W}_z \mathbf{W}(\mathbf{m} - \mathbf{m}_{ref})\|_2^2, \end{aligned} \quad (68)$$

where \mathbf{W}_s is a diagonal matrix, and \mathbf{W}_x , \mathbf{W}_y and \mathbf{W}_z are discrete approximations of the first derivative operator in x , y and z directions, respectively. The α 's are weighting parameters that balance the relative importance of producing small or smooth models. Model weighting matrix, \mathbf{W} is defined as

$$\mathbf{W} = \text{diag}(\mathbf{w}), \quad (69)$$

where \mathbf{w} is a column vector for weighting each model parameters.

5 Application: airborne time domain EM

In order to investigate the suggested methodologies to restore distributed IP parameters from the IP responses in airborne time domain EM (ATEM) problem, we compose an IP body model, which includes the IP body in the half-space as shown in Figure 7. Cole-Cole parameters of this IP body are fixed to $\eta = 0.2$, $\tau = 0.005$ and $c = 1$. Conductivity value of the half-space, (σ_1) is fixed to 10^{-3} S/m, whereas σ_∞ , which is same as σ_2 for the IP body varies. We have three different models, which we named canonical ($\sigma_2 = \sigma_1$), conductive ($\sigma_2 = 10^2 \times \sigma_1$) and resistive models ($\sigma_2 = 10^{-2} \times \sigma_1$). For the discretization of 3D earth, $50 \times 50 \times 50$ m core cell is used and the number of cell in the domain is $41 \times 41 \times 40$. The size of the IP body is $250 \times 250 \times 200$ m and the top boundary of this IP body is located at 50 m below the surface. In order to generate synthetic ATEM-IP data, we use EMTDIP code developed by [4]

Survey geometry include 11 soundings in each 11 lines as shown in Figure 7a. We use coincident-loop system and both Tx and Rx are located 30 m above the surface; the radius of the loop is 10 m. Step-off transmitter waveform is used and the range of the observed time channel is 0.01-10 ms. The observed responses can be either vertical component of \vec{b} or $\frac{\partial \vec{b}}{\partial t}$ fields. Based on this set up, in this section, first we analyze ATEM responses with IP effect and identify d^{IP} embedded in the observed data. Second, we validate approximations in our linearization idea by comparing \vec{j}^{IP} and \vec{j}_{approx}^{IP} . Furthermore, for the inverse problem, we will not recover pseudo-chargeability for each soundings but a representative pseudo-chargeability, which is same for every sounding. We also treat this issue while we are verifying our assumptions. Based on this validation, third, we apply linear inversion to each time channel of d^{IP} data separately and restore 3D distribution of pseudo-chargeability for each time channel. Finally, we investigate the possibility of extracting intrinsic IP parameters from pseudo-chargeability with deconvolution approach.

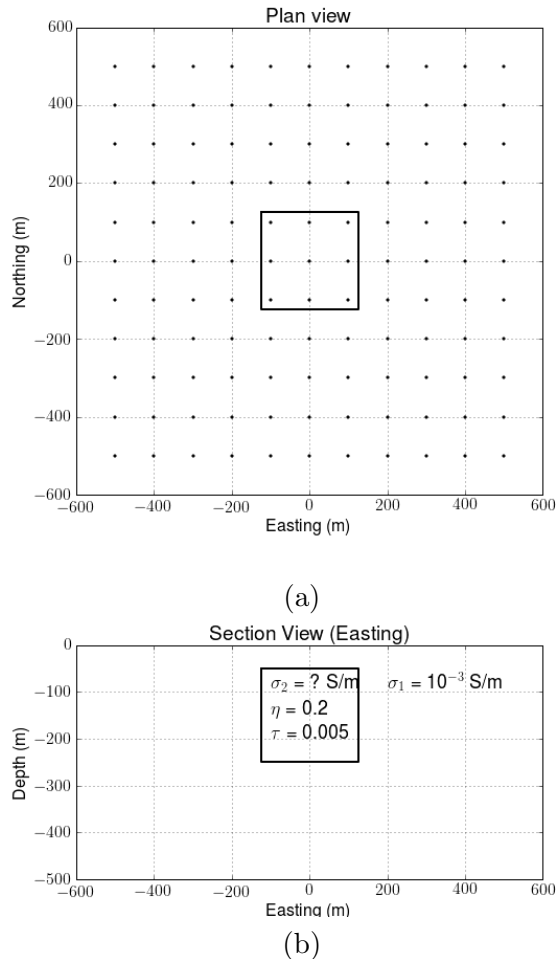


Figure 7: Plan (a) and section b) views of the IP model. Dashed line in (a) contours the boundary of the IP body. Solid circles in (a) denotes the location of stations.

5.1 Analyses of ATEM-IP responses

IP responses in ATEM data are different from different conductivity structure. Understanding different characteristics in IP response due to different conductivity can provide us important background physics. We use three different conductivity models: canonical, conductive and resistive. Then, we proceed EM decoupling approach, which subtract d^F from d , assuming that we know true conductivity (σ_∞), for all three cases and discuss features of IP response from different conductivity.

For the coincident loop system, the most clear IP response is negative transients. Simply, we consider that our ATEM data contain IP effects when we observe negative transients. For three different cases, we start with analyzing time decaying curves at the center sounding locations (0 m easting and 0 m northing). Figure 8 shows the observed (d), fundamental (d^F), and IP (d^{IP}) responses at the center sounding location for (a) canonical, (b) conductive and (c) resistive models. We provided both b_z (left panel) and $\frac{\partial b_z}{\partial t}$ (right panel). We focus on b_z in following studies because of its direct connection with the IP current shown in equation (51). Polarization charge build-up may have two main phases: charging and discharging. The IP current may increase in the charging phase, and decrease in the discharging phase. This phenomenon will be proportional on b_z^{IP} response thus, we choose a time when b_z^{IP} has maximum amplitude with negative values. The reason behind that we only use negative values to choose reference time is based on the background that the IP current has reversed direction to the reference current (49). This moment may indicate the time when the earth has the maximum polarization charge build up. Based on this time named as the reference time (t^{ref}), we divide charging and discharging phases. We first consider the canonical model ($\sigma_2 = \sigma_1$) shown in Figure 8a. In the observed data (d), we do not have any negative transients. However, due to the IP effect, the observed data shows rapid decay on late time channel after 1 ms. d^{IP} responses computed by the subtraction of d^F from d , have negative sign for all times, and the reference time is 0.1 ms. Even at this time, d^F is far greater than d^{IP} thus, EM induction is dominant. However, at late time after 1 ms, magnitude of d^{IP} response is considerable to that of d^F . $\frac{\partial b_z^{IP}}{\partial t}$ response show sign reversal from positive to negative at the reference time.

Second case has more conductive IP body than the background ($\sigma_2 = 10^2 \sigma_1$). As shown in Figure 8b, we observe negative transients after 1 ms. Compared to canonical model, fundamental response has greater amplitude in whole time range. The maximum amplitude of d^F is about 10^1 times greater than canonical case. In addition, d^{IP} response is greater than that of canonical case. The maximum d^{IP} is about 10^3 times greater than canonical case. The reference time occur at earlier time (0.05 ms) than canonical case (0.1 ms), and the gradients of d^{IP} on charging and discharging are much greater than canonical case. Similar to canonical case, $\frac{\partial b_z^{IP}}{\partial t}$ response show sign reversal at the reference time.

Third and last case is more resistive IP body than the background ($\sigma_2 = 10^{-2} \sigma_1$). Similar to the canonical case, the observed data does not have any negative values. The amplitude of the fundamental response is almost same as the canonical case. However, d^{IP} response show different phenomenon from the previous cases. d^{IP} has positive values at early time (0.01 ms), and shows sign reversal at 0.1 ms. The maximum amplitude of negative d^{IP} occurs at 0.4 ms. For the resistive case, there might be another level of complexity that we need to investigate based on the positive d^{IP} response at early time. We will clarify this phenomenon later by investigating the IP currents in the earth.

While analysis of time decaying curves at one sounding location provided time behaviour of ATEM-IP response, this does not provide the geometric features of IP anomaly from all sounding locations. In order to investigate the geometric features of d^{IP} response, we show maps of d , d^F and d^{IP} responses at early and late times from all sounding locations. Date

type here is b_z (nT). Left (d), middle (d^F) and right (d^{IP}) panels of Figure 9a shows maps for canonical model at the early time when $t = 0.03$ ms. Because the canonical model does not have any conductivity contrast, \vec{d} and d^F at this early time does not show any anomalous response. Although d^{IP} response exists in the observed data, relative strength of d^{IP} to d^F is much smaller. Figure 9b show three responses for conductive case. Due to induced vortex current, which increases total current, in the the conductive body, we can observe higher anomaly both on d and d^F at this early time. Compared to canonical case, d^{IP} map for conductive case shows more compact distribution. Figure 9c show three responses for resistive case. Due to the galvanic current, which reduces total current, both d and d^F have lower anomaly. This anomalous response compared to conductive case show more spreaded distribution. Different from both canonical and conductive cases, d^{IP} response for this case shows positive anomaly, which is consistent from the observation from transient curves. For all three cases at this early time, d^F is much greater than d^{IP} .

For the later time when $t = 7.08$ ms, we provided same maps in Figure 10. At this time d^{IP} is greater than d^F for all three cases. Although we do not observe any negative values on both canonical and resistive cases, by the EM decoupling process we can identify IP response embedded in the observation. Anomalous d^{IP} response for both canonical and resistive cases show more spreaded distribution than conductive case.

To summarize, the conductive case has the strongest IP signal due to the greater amplitude of d^F compared to other cases. b_z^{IP} response has minus sign for all time range except for the resistive case, and has charging and discharging phase. For the resistive case, d^{IP} shows positive values at early times. At certain late time, IP response is considerable to the fundamental one, whereas at the early time this is challenging because the fundamental response is dominant. Therefore, an effective time range for EM decoupling can be after certain late time when the IP response is considerable to the fundamental one. At the reference time when we may have maximum polarization charge build-up, $\frac{\partial b_z^{IP}}{\partial t}$ shows zero-crossing where sign reversal occurs for all three cases. d^{IP} response from conductive case show more compact distribution on map view compared to canonical and resistive cases.

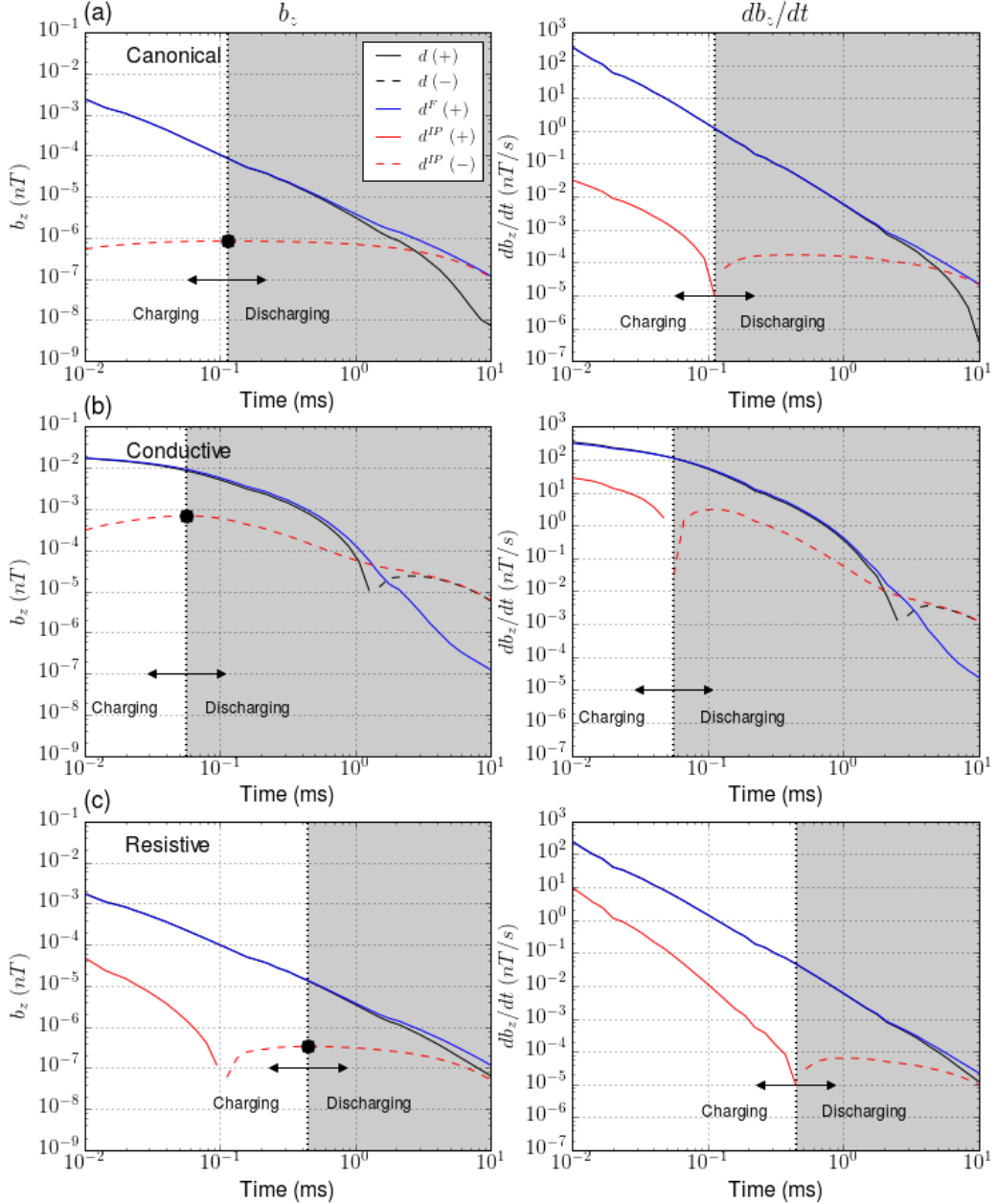


Figure 8: Time decaying curves of d (black line), d^F (blue line) and d^{IP} (red line) responses for three cases: (a) canonical, (b) conductive and (c) resistive. Right and left panels show b_z and $\frac{\partial b_z}{\partial t}$.

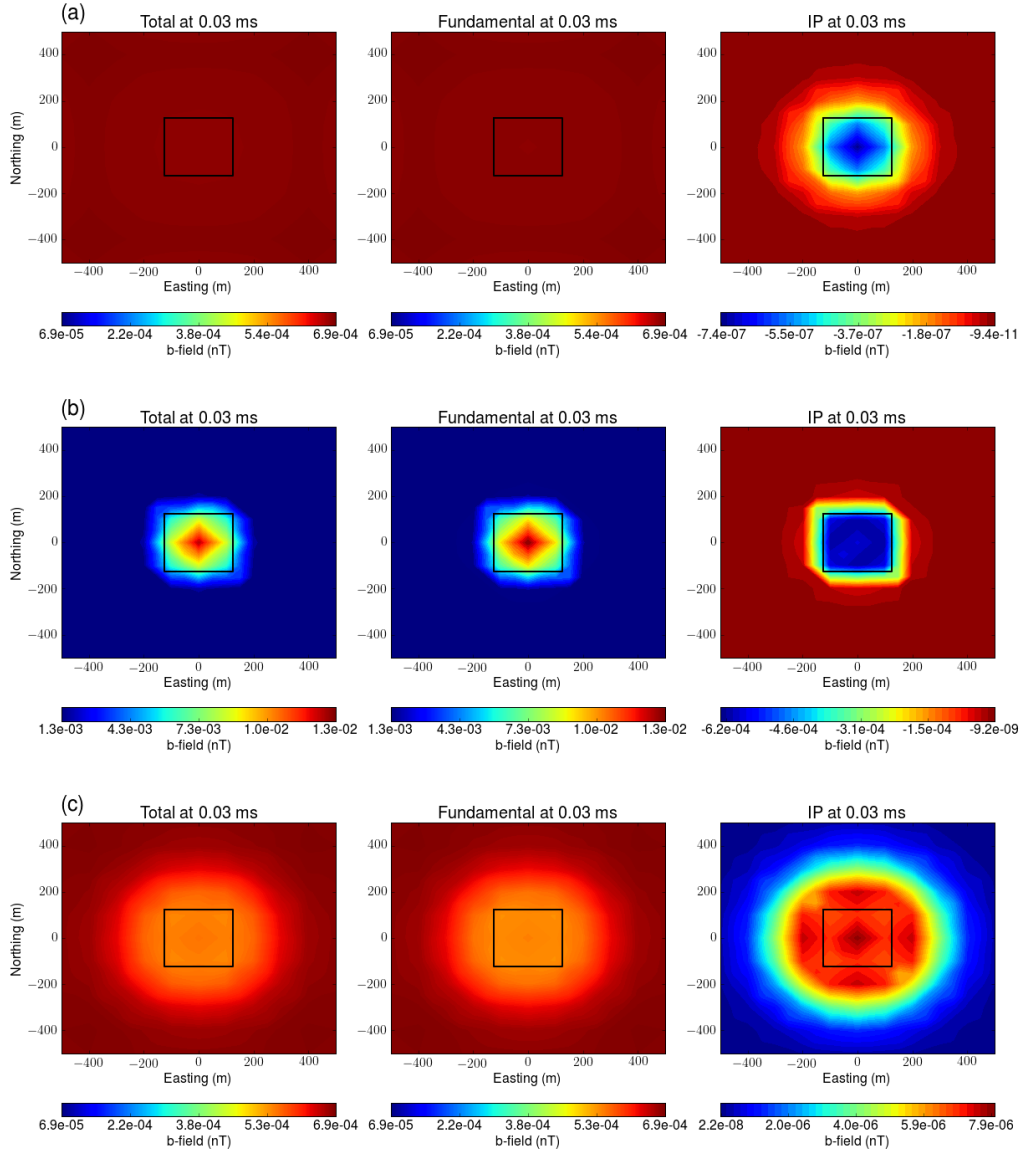


Figure 9: Response map of d (left panel), d^F (middle panel) and d^{IP} (right panel) at early time. Three maps for (a) Canonical, (b) conductive and (c) resistive cases are shown at 0.03 ms.

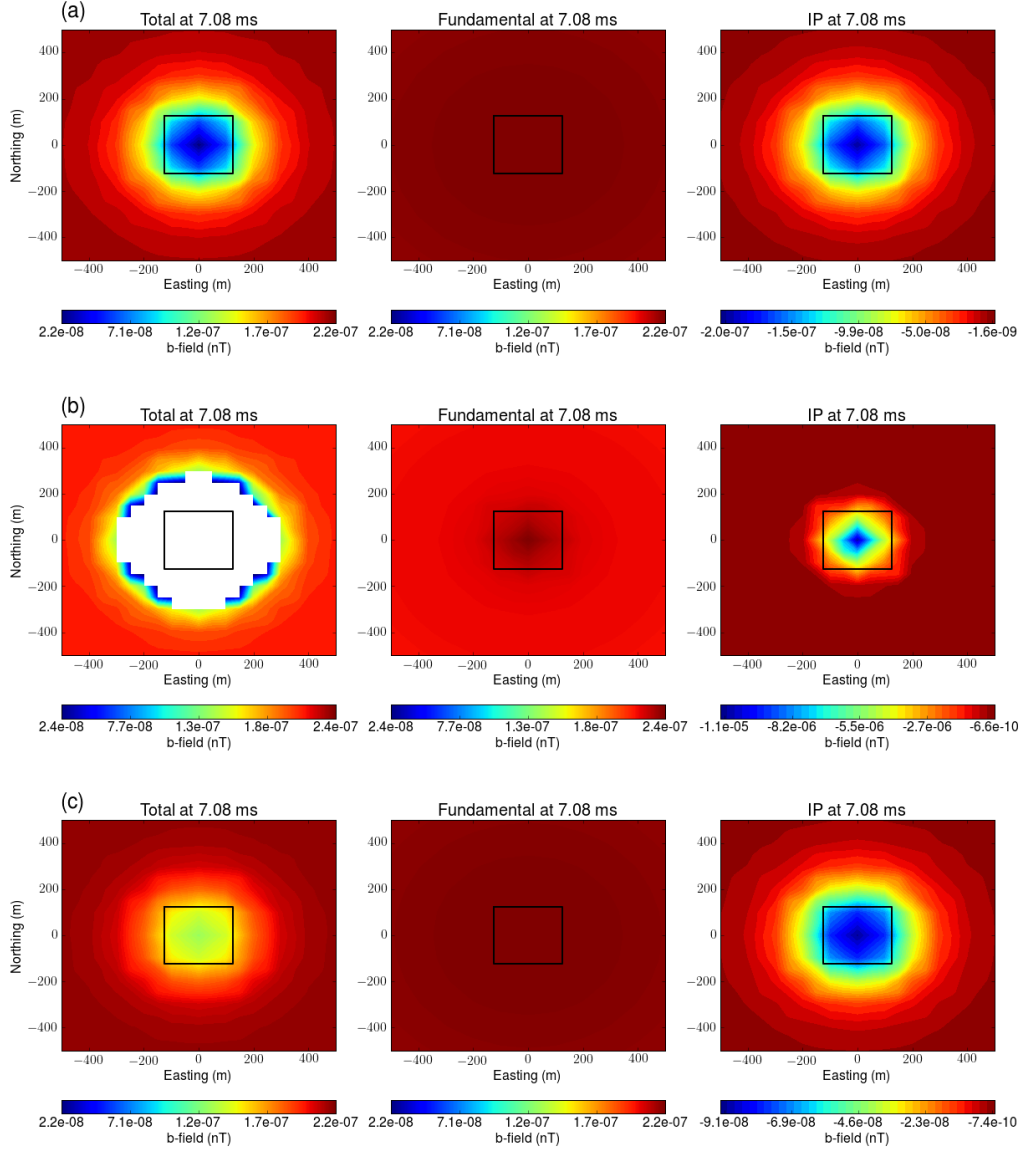


Figure 10: Response map of d (left panel), d^F (middle panel) and d^{IP} (right panel) at early time. Three maps for (a) Canonical, (b) conductive and (c) resistive cases are shown at 7.08 ms.

5.2 Analyses of IP currents

In previous section, we analyzed the IP responses for the three different conductivity models: canonical, conductive and resistive. Although we systematically analyzed IP response for each case, investigation of the IP currents in the earth can provide us more in-depth understanding of the IP phenomenon. In addition, we had one remainig question from the previous section: d^{IP} response for the resistive case has positive values at early time. This question possibly be related to different types of IP currents: galvanic (charge build-up) and vortex (EM induction) currents. Because these two currents have different geometric shape, we can easily recognize each effect by observing the IP current in the earth. Both currents will generate magnetic field at receiver locations. We investigate total, fundamental and IP currents where transmitter loop is located at (0 m, -200 m, 30 m).

Figure 11 shows plan view maps of total (left panel), fundamental (middle panel) and IP (right panel) currents at the early time (0.03 ms). Those currents for three different cases: (a) canonical, (b) conductive and (c) resistive are shown. From the equation (49), we can expect that the amplitude of the IP current may proportional to that of the reference currents. Direction of the IP current may be opposite to fundamental currents. Because the canonical case does not have conductivity contrast, the direction of the reference current may be similar to the fundamental current for all times. We can recognzie this expectation on three currents for the canonical case

From the geometric shape of the IP current, we recognize that the major effect of the IP current for this case is due to galvanic IP. For conductive case, we observe more localized fundamental current distribution in the conductive body. Vortex current generated in the conductive body has the same direction to fundamental current thus, this induced current increases total current. The IP current for this case show more compact distribution in the conductive IP body than canonical case, whereas the direction of the IP currents for both cases is similar at least have opposite directions to the fundamental currents. Similarly, the galvanic IP effect is dominant in conductive case. Different from the conductive case, the fundamental current for the resistive case show reduced amplitude due to the resistive body. Furthemore, the IP current has higher amplitude outside of the body, and the direction of the IP current has the opposite directions from those of the canonical and conductive cases. Especially near the transmitter location, which is outside of the body, we recognize the vortex IP current in the direction of the fundamental current thus, the IP current increases the total current. This observation shows the reason why we have positive IP response for the resistive case at the early time. For the resistive case, both galvanic and vortex IP currents has considerable amplitude. At this early time, IP currents for all three cases show two common features: a) amplitude of the IP current is much less than the fundamental current. b) galvanic IP effect is dominant in the IP current.

Figure 12, show the same three currents on plan view maps, but at the late time (7.08 ms). For all three cases, at this late time, the IP currents are dominant compared to the fundamental currents. Here, we recognize natural separation of EM and IP effects in time: EM effect is dominant in the early time, but decays faster than IP effect. Thus, we observe dominant IP effect at certain late time. Considering this, we recognize the effective time range of EM decoupling will be when the relative strength of IP effect is considerable to EM effect. Although it depends upon the conductivity structure and IP parameters of the earth, but this may commonly happen at certain late time channels in practice. Geometric shape of IP currents for canonical model did not change significantly, whereas that of the amplitude decays considerably. In addition, the galvanic IP effect is dominant even at this late time. This shows the similarity with EIP case because the geometric shape of the IP current will not change for

EIP case, although it decays in time. In contrast, the IP current for the conductive case show different characteristic. Different from the early time, in the body, we observe dominant vortex IP current in late time. The IP current for conductive case has much localized distribution compared to the IP current for canonical one. Geometric shape of the IP current for the resistive case at this late time significantly changed. Even the direction of the IP current at this late time is opposite to that at the early time. This clearly shows the sign reversal in the IP responses for this case. Similar to the early time both galvanic and vortex IP current has considerable magnitudes. In contrast, the amplitude of the IP current in the body is much smaller than that in the outside of the body, whereas the canonical and conductive case has higher amplitude in the body.

In summary, due to the natural separation of the EM and IP effects in time we can expect considerable IP effect in certain late time, and this is the time when we have some possibilities to recognize IP responses embedded in the observation. For the canonical model, the galvanic IP effect is the main driving force of the IP current. The IP current for the conductive case shows transition from galvanic to vortex currents as time increases. Both galvanic and vortex IP currents has considerable amplitude for the resistive case. Conductive case show the strongest amplitude of the IP current. Geometric shape of the IP currents for canonical case does not change significantly from early to late time, whereas those for the conductive and resistive cases show considerable changes in time.

5.3 Validation of linearization

5.3.1 IP current

To obtain a linearized kernel in equations (51), we approximate the IP current as a function of the pseudo-chargeability. Then by using Biot-Savart law, we evaluate d^{IP} response at the receiver location. To show the applicability of our approximate solution, we compare both the IP current and d^{IP} response for the approximate solution with those for the true one. We use the same three conductivity structures to investigate these comparisons. To compute the linearized kernel function, we need to choose the time when the amplitude of fundamental current reaches to the maximum for each pixel in 3D. This time and the current were called the maximum time (t^{max}) and current (\vec{j}_{max}^F). For all three conductivity models, we computed these \vec{j}_{max}^F and t^{max} (Figure 13). The maximum current for canonical case show vortex current, which is centered at the transmitter location. The maximum time for this case increases as the horizontal distance from the transmitter location increases. This makes sense because a closer pixel from the transmitter location will reach the maximum before a farther pixel does. Due to the conductivity contrasts in conductive and resistive models, \vec{j}_{max}^F and t^{max} show different features from those for the canonical case. The maximum current for the conductive cases shows the increased amplitude near the transmitter location. In addition, we observe the vortex current in the conductive body due to the induced vortex current in the history of time. This is clearly shown in t^{max} : in the body, the current reaches to the maximum on later time. In contrast, for the resistive case, the amplitude of \vec{j}_{max}^F is decreased both near the transmitter and in the body. Because of its resistive nature, the current reaches to the maximum time at earlier time in the body. Considering the assumption we made for the polarization current: $\vec{j}^{pol}(t) = -\vec{j}_{max}^F \tilde{\eta}(t)$, we can recognize that the effect of different conductivity structure in the IP current can be captured through \vec{j}_{max}^F .

Using these maximum currents for each case with the equation (49), we can compute the approximate IP current (\vec{j}_{approx}^{IP}). We compare the true and approximate \vec{j}^{IP} . Figures 14 and 15 show the comparisons of the true and approximate IP currents on plan view maps at the early (0.03 ms) and late (7.08 ms) times, respectively. In addition, we plotted time decaying

curves of total, fundamental and those two IP currents in y -direction at a single pixel in the body (noted as Rx in the figures) on Figure 16 for canonical (a), conductive (b) and resistive (c) models. Thick dashed and solid lines indicate the early and late times used on above plan view maps. The true and approximate IP currents for the canonical case almost coincident not only on plan view maps at this late time (7.08 ms), but also on the early time as shown in Figures 14 and 15. Furthermore, the time decaying curves of these IP currents are almost coincident on all times as shown in Figure 16. Thus, for the canonical case, our assumptions on the IP current is reasonable for all time range. For the conductive case, at the late time, true and approximate IP currents show reasonable match, whereas they show significant difference at the early time (Middle column of Figures 14 and 15). The approximate IP current for the conductive case converges to the true one near 2 ms (Figure 16b) thus, our approximate solution is reasonable near this time for conductive case. Different from two previous cases, the IP current for resistive case have greater amplitude on the outside of the body. At the early time, the approximate solution show significant difference from true one. Even at the late time, the amplitude of true and approximate IP currents show considerable difference on the outside of the body. However, those for inside of the body show reasonable match. In addition, the direction of the true and approximate IP currents are almost identical at the late time. We summarized above comparisons in Figure (17). A principal assumption that we made for the polarization current was $\vec{j}^{pol}(t) \approx \vec{j}_{max}^F \tilde{\eta}(t)$. The observation that the approximate IP current in the body show good approximation for all three cases at late time suggests that the above approximation is reasonable after a certain the late time when the amplitude of the IP current is considerable to that of the fundamental current. At this late time period, the approximate IP current show good match with true one for all three cases except for the amplitude of resistive case. This makes the applicability of the linearized kernel function somewhat arguable for the resistive case.

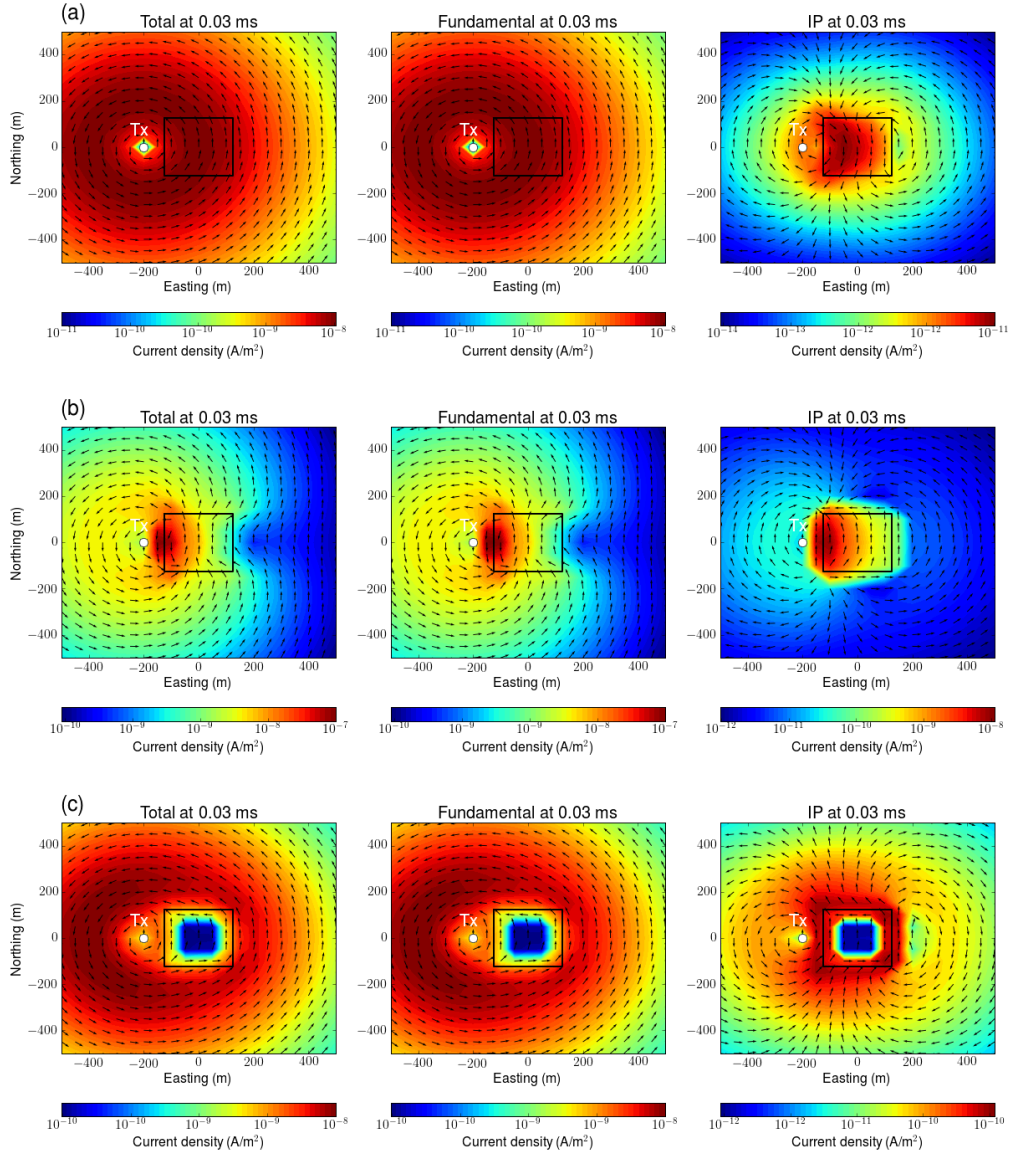


Figure 11: Maps of total, fundamental and IP currents at early time. Three maps for (a) Canonical, (b) conductive and (c) resistive cases are shown at 7.08 ms.

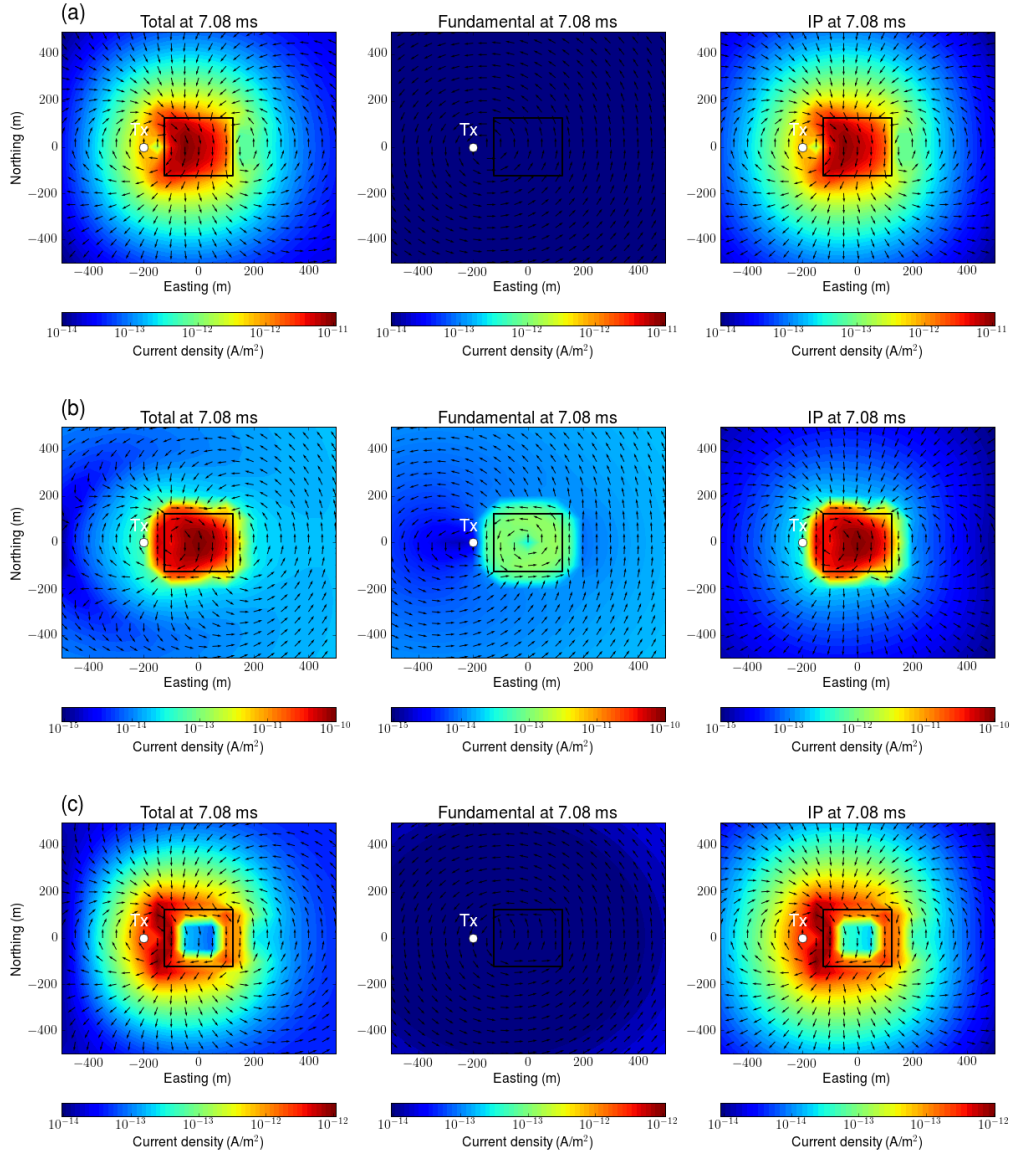


Figure 12: Maps of total, fundamental and IP currents at early time. Three maps for (a) Canonical, (b) conductive and (c) resistive cases are shown at 7.08 ms.

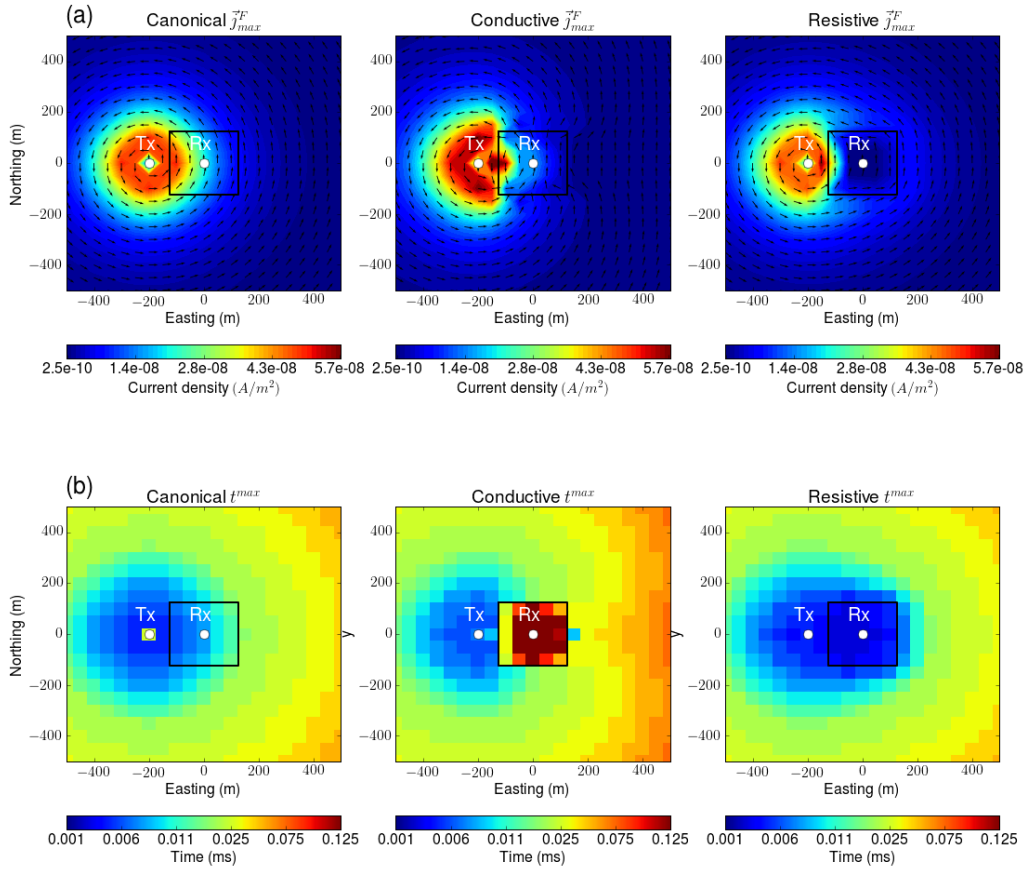


Figure 13: Plan view maps of \vec{j}_{max}^F (a) and t^{max} (b) at -125 m depth. Left, middle and right panels correspondingly show those for canonical, conductive and resistive models.

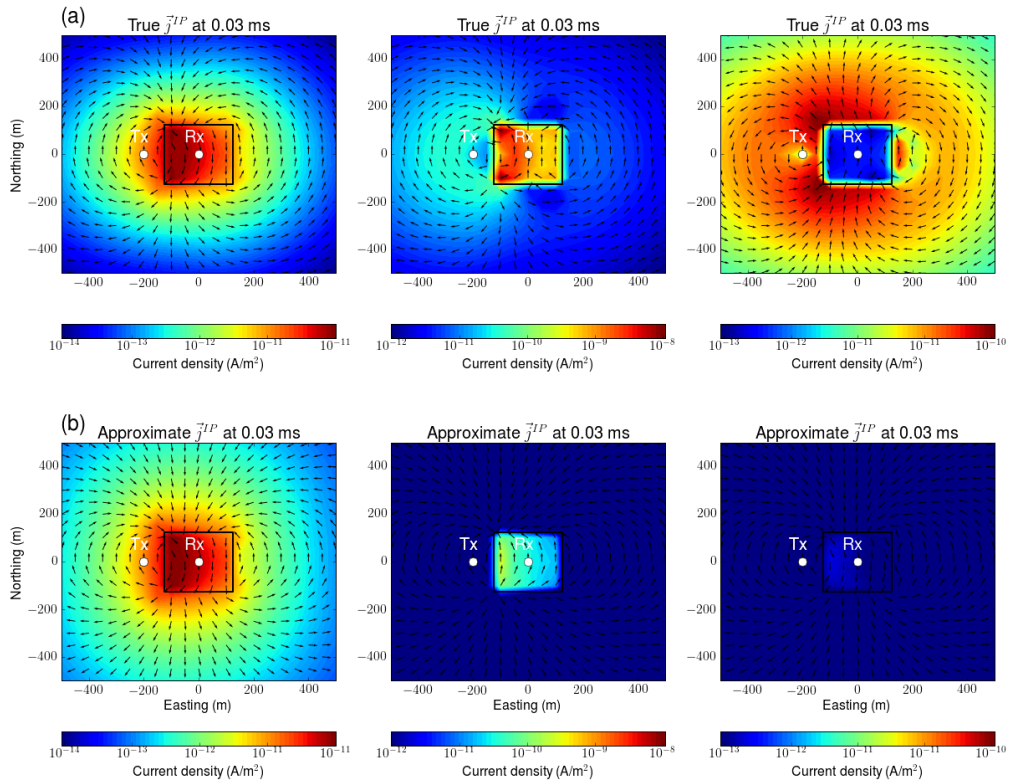


Figure 14: Plan view maps of the true (a) and approximate (b) \vec{j}^{IP} at -125 m depth and $t=0.03$ ms. Left, middle and right panels correspondingly show those for canonical, conductive and resistive models.

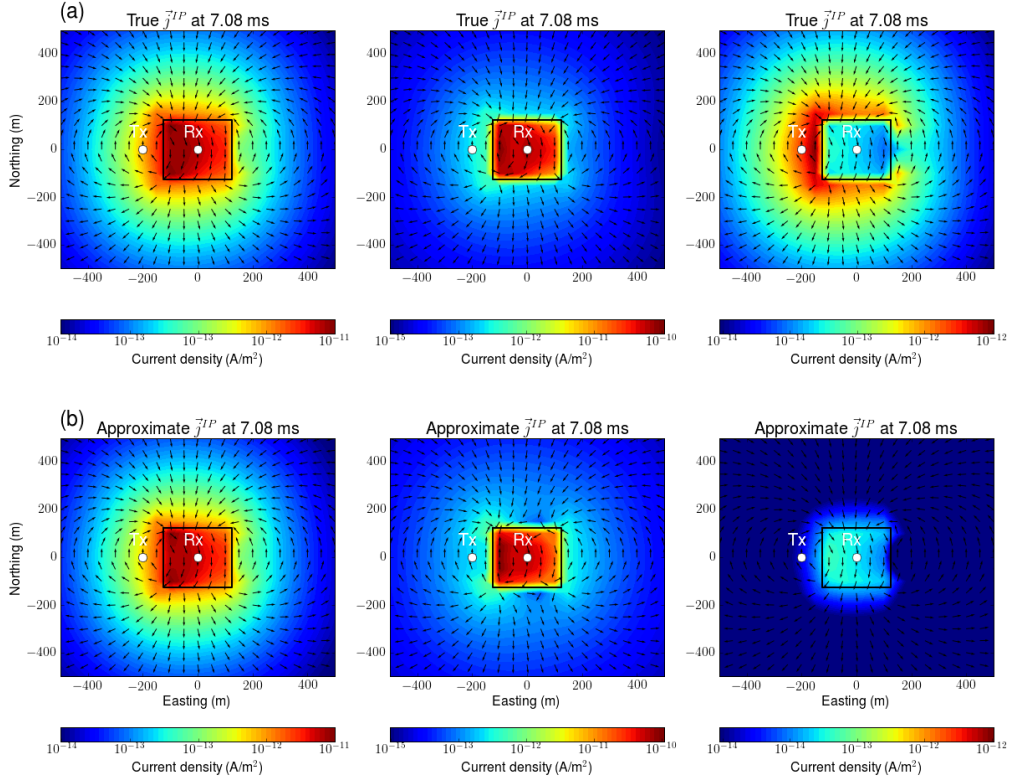


Figure 15: Plan view maps of the true (a) and approximate (b) \vec{j}^{IP} at -125 m depth and $t=7.08$ ms. Left, middle and right panels correspondingly show those for canonical, conductive and resistive models.

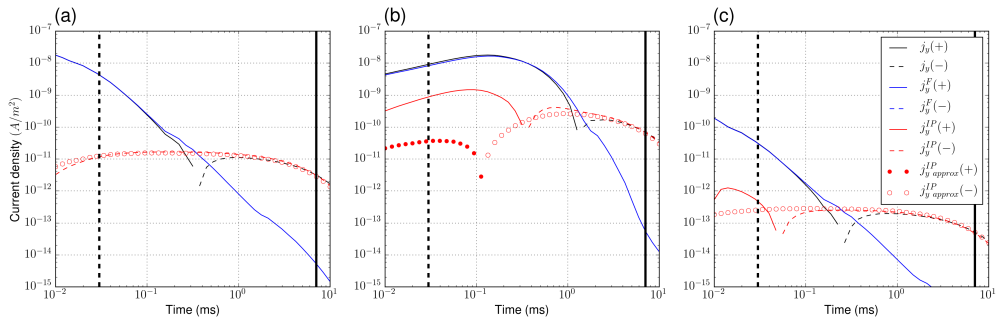


Figure 16: Plan view maps of the true (a) and approximate (b) \vec{j}^{IP} at -125 m depth. Left, middle and right panels correspondingly show those for canonical, conductive and resistive models.

Division	Canonical		Conductive		Resistive		
	Direction	Amplitude	Direction	Amplitude	Direction	Amplitude	
Early	Good	Good	Good	Poor	Poor	In	Out
						Poor	Poor
Late	Good	Good	Good	Good	Good	Good	Poor

Figure 17: Comparisons of the applicability of the approximate IP currents for three different cases: canonical, conductive and resistive conductivity models.

5.3.2 IP response

Although the IP current is the core of the linearized kernel function, the output of this function is d^{IP} response, which was evaluated by using Biot-Savart law with the approximate IP current. In order to validate the linearized kernel, we also need to compare d^{IP} response generated by the linearized kernel function with the true d^{IP} response, which is computed by subtraction process shown in equation (26). Because we use the coincident loop system the receiver location is same as the transmitter location. The data type we chose in our example is a vertical component of magnetic flux density (b_z^{IP}). To show the reliability of applying Biot-Savart law, we also plotted b_z^{IP} response computed by using Biot-Savart law ($b_z^{IP,BS}$) with the true IP current. As shown in Figure 18, they are almost identical to true b_z^{IP} . In the same figure, we compare the true and approximate d^{IP} responses for three cases. The true and approximate IP responses for the canonical model (black) shows good match on all times except for very early time (0.01 ms). The approximate IP response for the conductive case (blue) converges to the true one as we go to the later time, whereas they show significant difference on early time. This is consistent result with the phenomenon on the approximate IP current of the conductive case. The true and approximate IP responses for the resistive case show considerable difference for all times due to the poor amplitude of the approximate IP current.

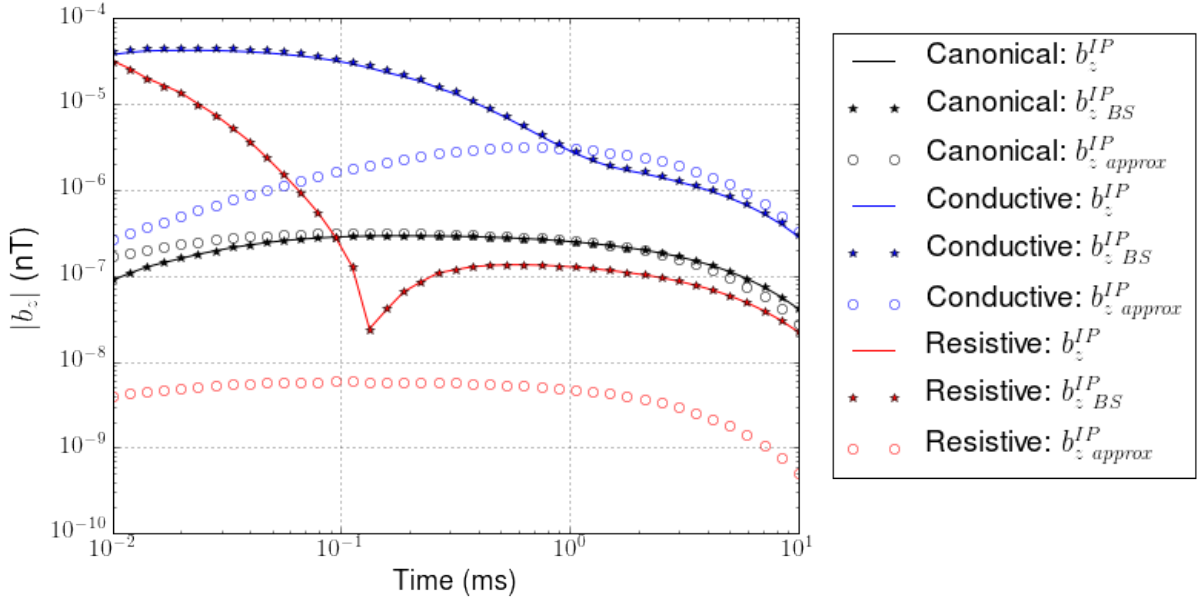


Figure 18: Comparison of true and approximate d^{IP} responses. The data type here is vertical component of the magnetic flux density (b_z). Black, blue and red color correspondingly stand for canonical, conductive and resistive cases.

5.3.3 Discussion for the resistive case

Comparisons of the true and approximate solutions for the IP current and response suggest that our linearized kernel function is reasonable at certain late time except for the resistive case. This is mostly resulted from the poor approximation for the amplitude of the IP current. Then why the approximate IP current lose the amplitude? We try to explain this phenomenon by decomposing the IP current as three parts:

$$\vec{j}^{IP} = \vec{j}^{pol} - \vec{a}_J^{IP} - \vec{\nabla}\phi_J^{IP}, \quad (70)$$

where $\sigma_\infty \vec{e}^{IP} = -\vec{a}_J^{IP} - \vec{\nabla}\phi_J^{IP}$. This is Helmholtz decomposition of $\sigma_\infty \vec{e}^{IP}$ thus, $\nabla \cdot \vec{a}_J^{IP} = 0$. Because we recognized that our approximation for \vec{j}^{pol} is good, a possible source of the reason why our assumption show poor performance for the resistive case, is $\sigma_\infty \vec{e}^{IP}$. In addition, considering Biot-savart law shown in equation (32), computed \vec{b}^{IP} does not affected by $\vec{\nabla}\phi_J^{IP}$ because it is curl-free component. Therefore, if the relative strength of \vec{a}_J^{IP} is greater than \vec{j}^{pol} , the approximate IP current may not describe the amplitude of the true IP current and this will induce same effect on the approximate d^{IP} response. Figure 19 show \vec{j}^{pol} , $-\vec{a}_J^{IP}$ and $-\vec{\nabla}\phi_J^{IP}$ for all three cases at 7.08 ms. The amplitude of the polarization current for canonical and conductive cases at this late time are greater than those of \vec{a}_J^{IP} and $\vec{\nabla}\phi_J^{IP}$. However, in the resistive case, the amplitude of \vec{a}_J^{IP} is greater than that of \vec{j}^{pol} . This shows the reason why our approximation has poor description for the amplitude of the true IP current and d^{IP} response in the resistive case.

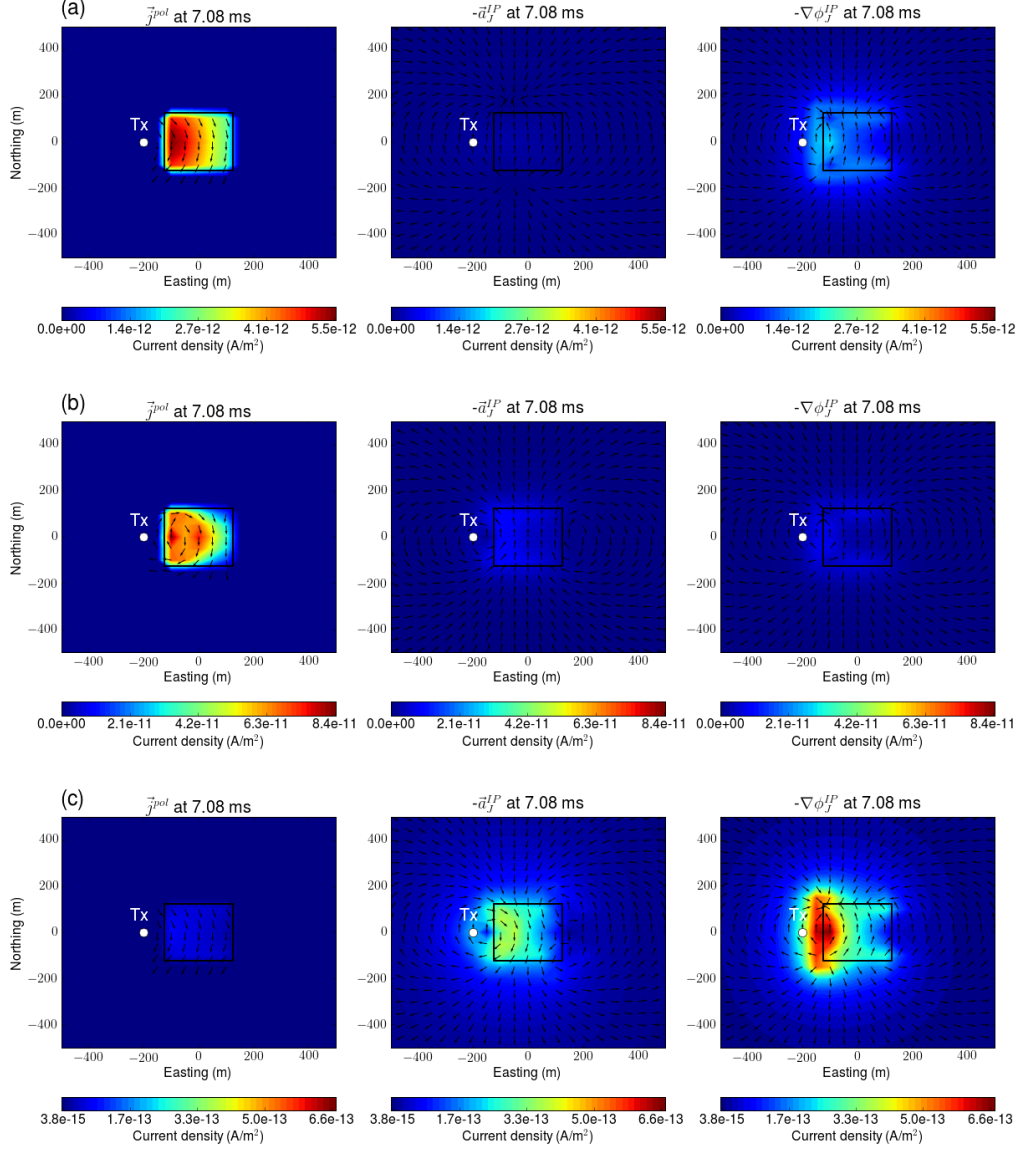


Figure 19: Plan view maps of the true (a) and approximate (b) \vec{j}^{IP} at -125 m depth and $t=7.08$ ms. Left, middle and right panels correspondingly show those for canonical, conductive and resistive models.

5.4 A potential for recovering IP parameters

Although the physical understanding of the linearized kernel function is important, our final goal will be the IP inversion of the ATEM data. To investigate a potential of this task, we extract intrinsic IP parameters from a single pixel of the pseudo-chargeability, which is located at the center of the IP body (marked as Rx on Figures 15). Recalling that the pseudo-chargeability is the convolution between $\tilde{\eta}^I(t)$ and $w^e(t)$ (43), we need to solve a deconvolution problem to extract intrinsic IP parameters including η and τ . Since we consider Debye case ($c = 1$) for Cole-Cole model, we assume that we know c . Definition of the intrinsic pseudo-chargeability is shown in equation (4). We compute $\tilde{\eta}$ and w^e for all three cases to make a synthetic data for this deconvolution problem. Using a conventional deconvolution problem, which directly recover impulse response, we can recover $\tilde{\eta}^I(t)$. However, we are more interested in Cole-Cole parameters including η and τ . Accordingly, we set these two IP parameters as our inversion model. Using the Gauss-Newton method, we optimize this problem and recover these two parameters. We consider the pseudo-chargeability at a single pixel as the observed data, and convolution between $\tilde{\eta}^I(t)$ and $w^e(t)$ as a forward problem. Figure 20a and b show $w^e(t)$ and comparisons of the observed and predicted data. Because $w^e(t)$ can be considered as the normalized time history of the electric field, for all cases it starts from zero and increases until it reaches to the peak. After that it decays. Resistive case reaches to the maximum at the earliest time. Canonical and conductive cases reach at the maximum almost same time, although the conductive case show much slower decay after this time. Those phenomenon make sense considering their conductivity features in terms of the EM induction. As shown in Figure, recovered τ and η are same as true ones, and the observed and predicted data show good matches. The true τ and η for all three cases were 0.005 and 0.2, respectively. Considering the approximate IP currents in the body for all three cases showed good match with the true ones (Figure 16), we can recognize the potential for recovering intrinsic IP parameters from airborne time domain EM data.

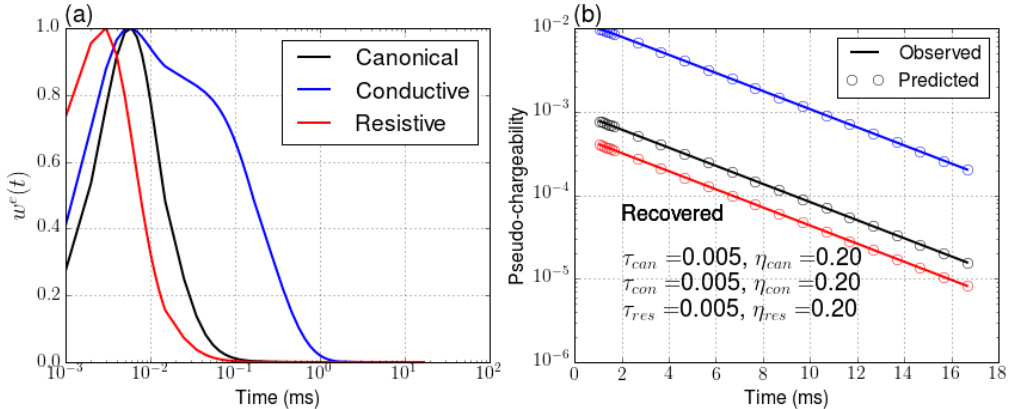


Figure 20: (a) The normalized time history of the fundamental electric field ($w^e(t)$) for all three cases. Black, blue and red colors correspondingly indicate canonical, conductive and resistive cases. (b) Comparisons of the observed (line) and predicted (empty circles) pseudo-chargeability at the center pixel in the IP body for three cases.

5.4.1 Validation for an equivalent pseudo-chargeability

For the 3D IP inversion using the linearized kernel function, we assume an equivalent pseudo-chargeability (equation (64)). If the $w_k^e(t)$ for each sounding is same, our assumption is true as shown in equation (63). To investigate this, we choose four sounding locations along the profile

line at Norting 0 m, which are located at Easting -400, -300, -200 and -100 m. The normalized time history of the electric field at the center pixel of the IP body for those four soundings are shown in Figure 21. In this figure, those for canonical (a), conductive (b), and resistive (c) cases are shown. For all three cases the time for the maximum amplitude delays as the sounding location gets farther from the IP body. Similar to the observation from Figure 20, the order for the most delayed peak time is 1) conductive, 2) canonical, and 3) resistive. Although the peak amplitude of the w_k^e for four soundings are same as 1, delayed peak time of w_k^e are different for four soundings. Therefore, our assumption of the equivalent pseudo-chargeability for the ATEM case can be arguable. For the clear manifestation of this issue, we set up a validation procedure: a) we evaluate $\tilde{\eta}_k(t)$ from all soundings. Considering the definition of d^{IP} datum (equation 53), (b) we only select several soundings (8 or 9), which has greater product of pseudo-chargeability and Jacobian (P-J product) at the center pixel of the IP body. (c) We compute averaged w^e and $\tilde{\eta}$ using w_k^e and $\tilde{\eta}_k$ for those selected soundings. Finally, (d) we evaluated d^{IP} responses for every sounding using this averaged $\tilde{\eta}$, and compare these with true d^{IP} responses. Using w_k^e , we computed $\tilde{\eta}_k$ for all sounding locations at 7.08 ms. Figure 22 shows those $\tilde{\eta}_k$ for all three cases. Because 7.08 ms is after the time for the peak amplitude of $w_k^e(t)$, we observe increasing pseudo-chargeability farther from the IP body. Figure 23 shows, P-J product for all three cases at the same time. We chose 8 soundings for the canonical and resistive cases, and 9 soundings for the conductive case considering the symmetry of the selected soundings. Selected sounding locations are marked as empty circles on both Figures 22 and 23. Selected soundings are located near the IP body for all three cases, whereas the conductive case show different pattern for the selected sounding locations from two other cases due to the dominant vortex current induced in the IP body. We compute averaged w^e and $\tilde{\eta}$ using the selected soundings. Figure 24 show averaged w^e (a) and $\tilde{\eta}$ (b) at the center pixel of the IP body for canonical (black), conductive (blue), and resistive (red) cases. Using the averaged $\tilde{\eta}$, we evaluate approximate d^{IP} response. Figures 25 shows comparison of the true and approximate d^{IP} response at 7.08 ms with the Rx number plot. True (black dot with line) and approximate (empty circle) d^{IP} responses show reasonable match except for the resistive case. The magnitude of the approximate d^{IP} response is much less than the true one, which is consistent result from Figure 18. To investigate the reliability of the approximate d^{IP} response in terms of geometry, we provided plan view maps of them. Figure 26 show plan view maps of the true (a) and approximate (b) d^{IP} responses for the canonical (left panel), conductive (middle panel), and resistive (right panel) cases. Here we did not set the range of the colorbar same to better recognize the geometry of the responses. For all three cases, the geometry of the approximated d^{IP} response are similar to the true ones. Even for the resistive case, the geometry of the approximate d^{IP} response is reasonable, although its magnitude is much smaller than true one. Based on this, we can expect that the magnitude of the recovered pseudo-chargeability from the resistive case may be much greater than the true one, whereas its geometry may be reasonable. Above analyses support the reliability of the equivalent pseudo-chargeability (equation (64)) for ATEM case.

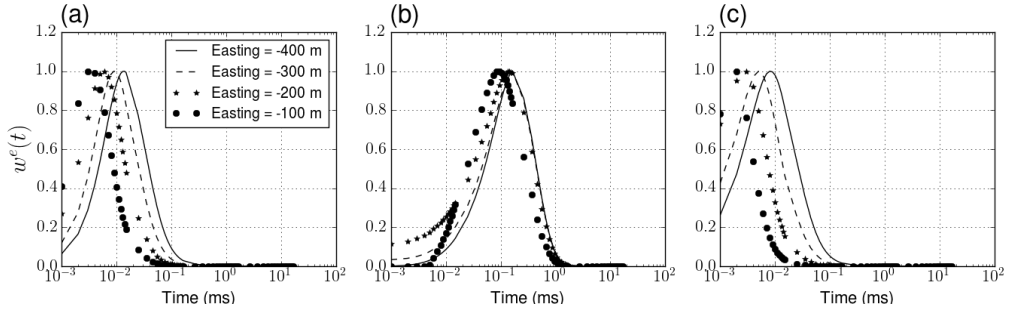


Figure 21: The normalized time history of the electric field ($w^e(t)$) at the center pixel of the IP body for (a) canonical, (b) conductive, and (c) resistive cases. Solid lines, dashed lines, stars and solid circles indicate four different transmitters located at Easting -400, -300, -200 and -100 m along the profile line at Northing 0 m.

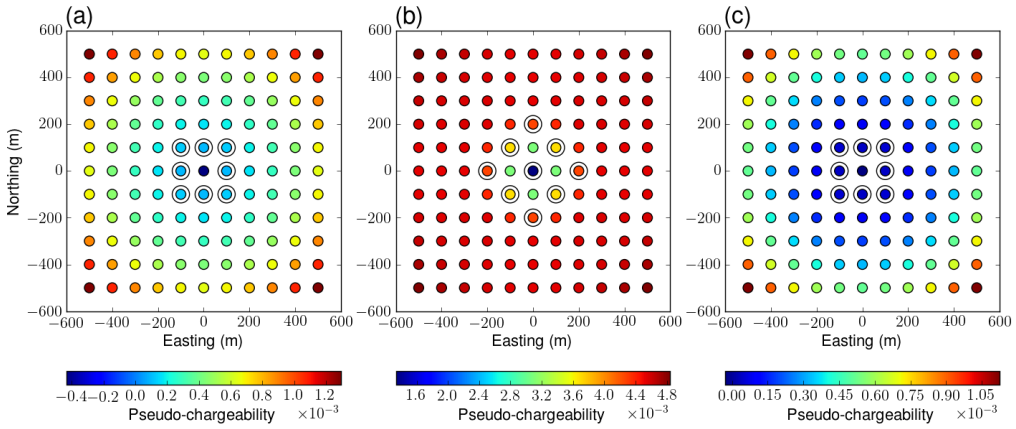


Figure 22: Pseudo-chargeability on the center pixel of the IP body at 7.08 ms for all soundings. Canonical (a), conductive (b), and resistive (c) cases are shown. Empty circles indicate the selected sounding locations to compute averaged pseudo-chargeability.

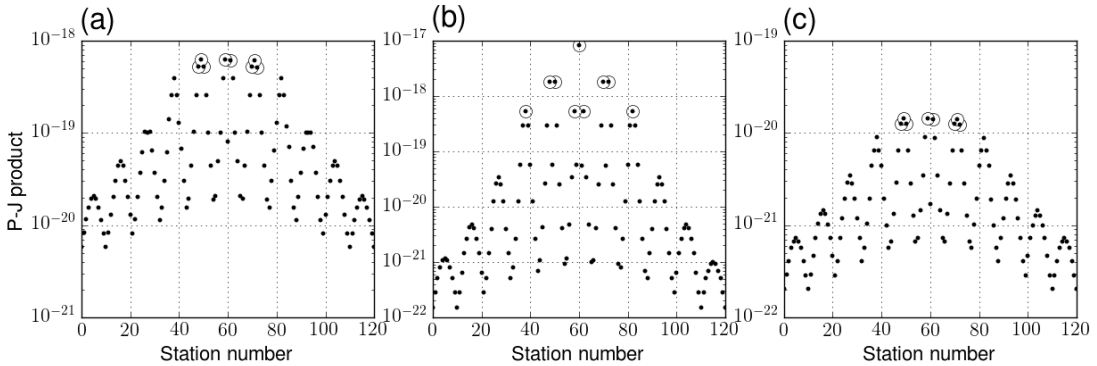


Figure 23: Pseudo-chargeability and Jacobian (P-J) product at the center pixel of the IP body ($t = 7.08$ ms) for all soundings. Canonical (a), conductive (b), and resistive (c) cases are shown. We chose top eight (canonical and resistive cases) or nine (conductive case) greatest amplitude of the P-J product from all sounding locations considering the symmetry on the plane (See Figure 21), and marked these as empty circles.

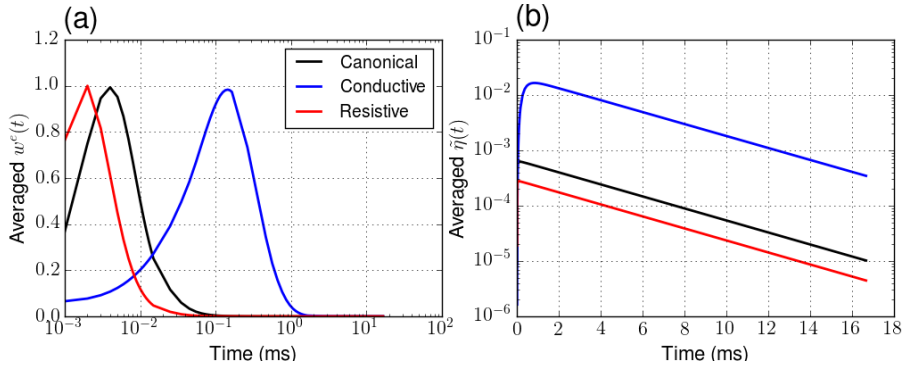


Figure 24: Averaged (a) w^e and (b) $\tilde{\eta}$ from the selected sounding locations shown in Figure 21.

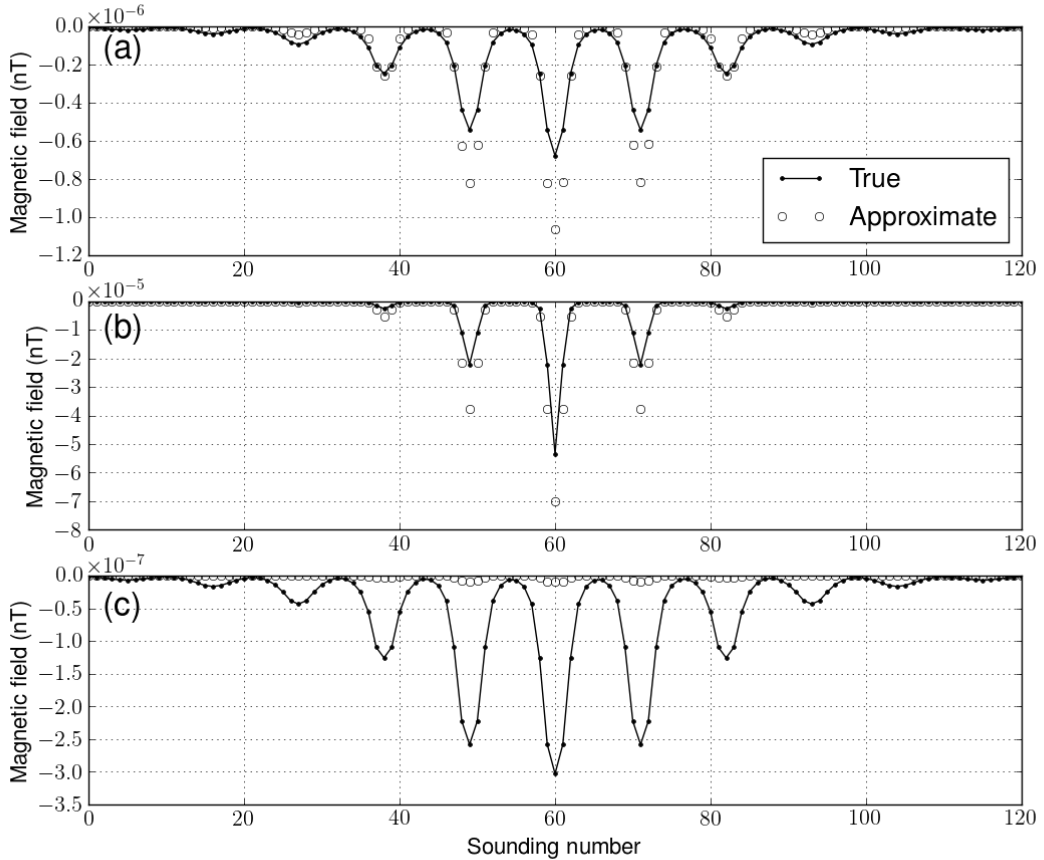


Figure 25: Comparison of true (solid circle with line) and approximate (empty circles) b_z^{IP} responses at 7.08 ms as a function of sounding number. Canonical (a), conductive (b) and resistive (c) cases are shown.

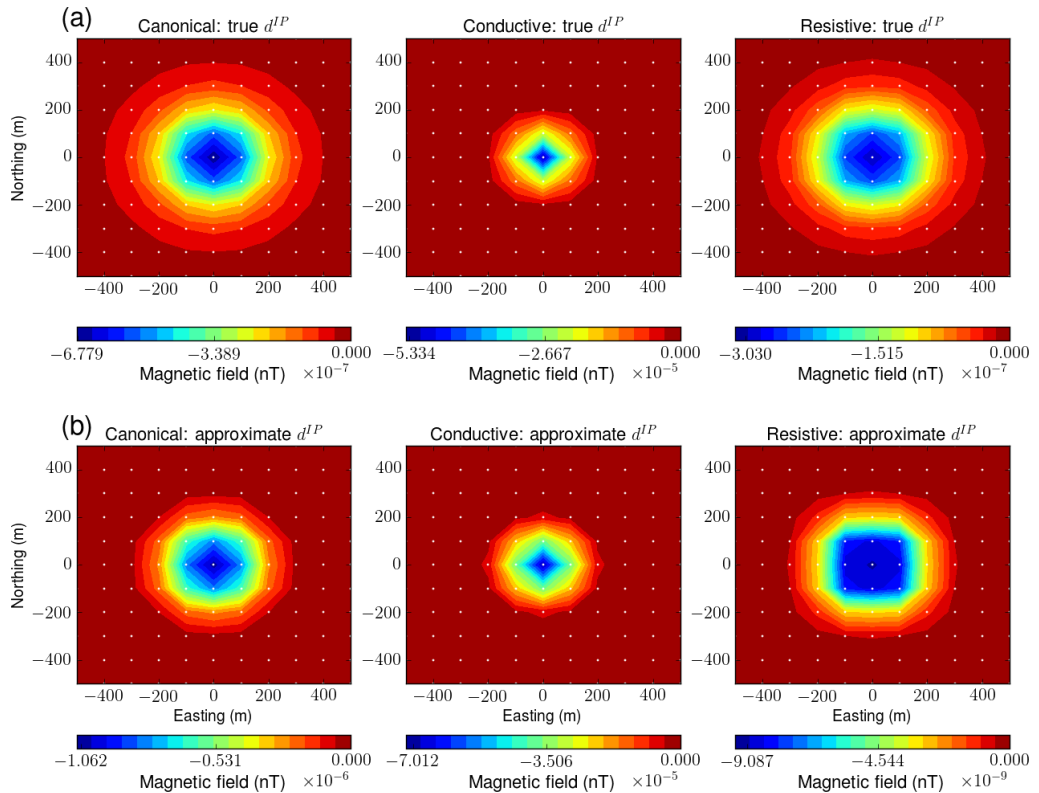


Figure 26: Comparison of true (a) and approximate (b) b_z^{IP} responses at 7.08 ms on plan view map. Canonical (left column), conductive (middle column) and resistive (right column) cases are shown.

5.4.2 Depth weight and positivity on pseudo-chargeability

Based on the linear relationship shown in equation (51), any time-dependency in our approximate d^{IP} response is originated from the pseudo-chargeability ($\tilde{\eta}(t)$), thus the sensitivity function is purely geometric. Furthermore, we are inverting each time of d^{IP} response, separately. Therefore, we can expect that our 3D inversion method for typical ATEM data, which has a transmitter-receiver pair may not have intrinsic depth resolution like TEM inversion due to the lack of time-sounding information. However, similar to the magnetic or gravity inversions, we may expect relative depth resolution with a depth weighting (CITE). In order to investigate the effect of depth weighting and depth resolution in the 3D IP inversion, we use the canonical model and approximate d^{IP} response generated by the linear kernel function shown in equation (51). We set the synthetic equivalent pseudo-chargeability ($\tilde{\eta}_{eqv}$) as one in the IP body and zero on outside of the body. The 3D IP inversions are applied to approximate d^{IP} response with and without depth weighting. Based on the depth weighting used in the magnetic inversion (CITE), we use $\mathbf{w} = (\mathbf{z} - \mathbf{z}_0)^{-1.5}$ as the discretized weighting function shown in equation (69).

Left and right panels of Figure 27 show the inverted pseudo-chargeability sections with and without depth weight, respectively. Without the depth weighting, inversion puts higher pseudo-chargeability anomaly on the near surface because of much greater sensitivity than in the deeper part of the earth. Using the depth weighting, the 3D IP inversion imaged the IP body on reasonable depth. In both cases, data misfit reached to the target misfit. To test the relative depth resolution of the IP inversion, we put the IP body 50 m deeper than before. Figure 28 compares inverted pseudo-chargeability sections of two different models with different depths of the IP body. A cell, which has maximum pseudo-chargeability is lowered on the recovered pseudo-chargeability section for the deeper IP body case. Although, synthetic tests that we have been made so far is in idealistic situation, results of these tests suggest that the 3D IP inversion of the ATEM data has potential to distinguish relative depth of the IP bodies in the earth with the depth weighting.

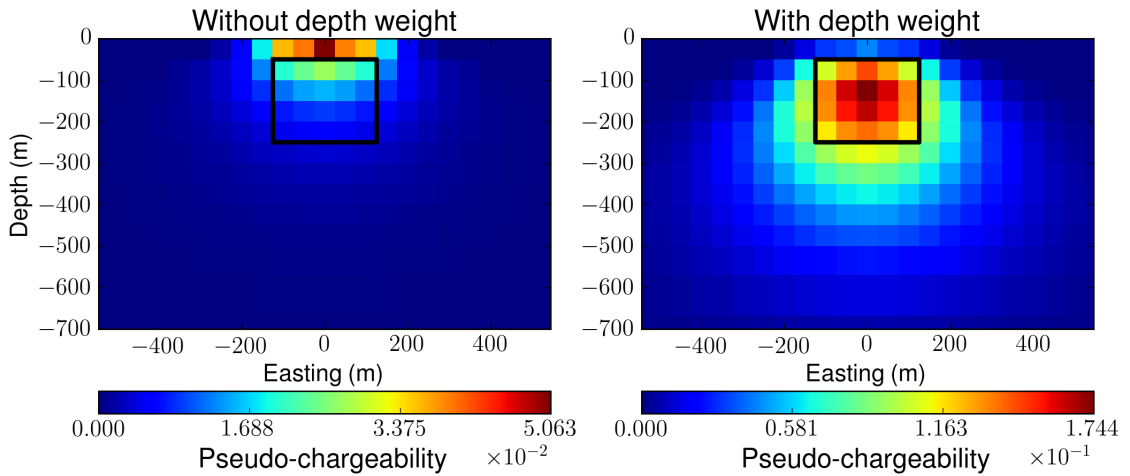


Figure 27: Comparison of the recovered pseudo-chargeability model without (left panel) and with (right panel) on vertical section at Northing 0 m. Black solid line indicate boundary of the IP body.

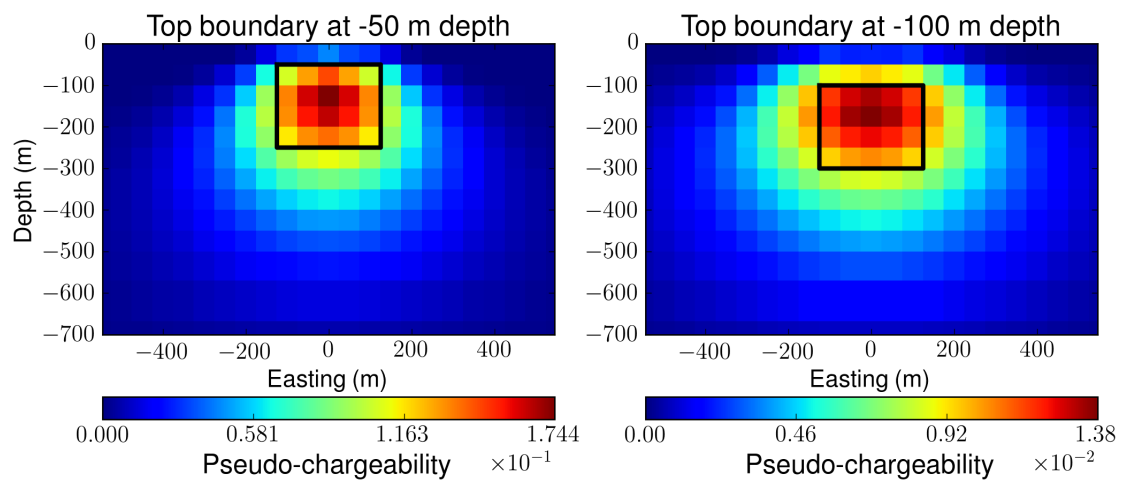


Figure 28: Comparison of the recovered pseudo-chargeability models from variable depths. The depth for the top boundary of the IP body varies from -50 m (left panel) to -100 m (right panel).

5.4.3 Incorrect conductivity mode with positivity constraint

A principal assumption that we have made on the 3D IP inversion for the ATEM data is the knowledge of 3D distribution of σ_∞ model in the earth. However, this is definitely not known information in practice. On our IP inversion procedure, we apply 3D ATEM inversion to recover this conductivity model with the exception of the IP contaminated data. Assuming that we have some early time responses, which are not contaminated by the IP effect, we can recover reasonable σ_∞ model. However, this is still different from the true σ_∞ model thus, our conductivity model for the IP inversion is incorrect. The effect of this incorrect conductivity model can exist on two main places: fundamental response (CITE) for the EM decoupling and sensitivity function (CITE). In order to investigate both effects, we use the conductive IP model, thus, the conductivity of the half-space (σ_1) and the IP body (σ_2) are 10^{-3} and 10^{-1} S/m, respectively. To investigate the effect of the incorrect conductivity on the EM decoupling, we perturbed the conductivity of the half-space (σ_1) as $2 \times \sigma_1$ and $0.5 \times \sigma_1$, and computed three fundamental responses from these three conductivity models with σ_1 , $2 \times \sigma_1$, and $0.5 \times \sigma_1$. By subtracting these three fundamental responses from the observed responses shown, we computed d^{IP} responses. Figure 29 shows those three d^{IP} responses with σ_1 , $2 \times \sigma_1$, and $0.5 \times \sigma_1$ on Easting profile line (Northing 0 m) at 0.3 ms. Compared to the magnitude of the true d^{IP} responses, that of the perturbed d^{IP} responses with $2 \times \sigma_1$ and $0.5 \times \sigma_1$ are over-estimated and under-estimated, respectively. Therefore, both d^{IP} responses (d_{obs}^{IP}) computed from the perturbed conductivity models include residual field ($\Delta d[\sigma_\infty] = d_{obs}^{IP} - d^{IP}$). We need to remove this residual field in d_{obs}^{IP} , and this process is called as regional removal. Although this can be significantly important procedure in practice, we do not treat this processing in this section. Rather we focus on identifying the effect of this regional field on the recovered pseudo-chargeability model.

We apply the 3D IP inversions to those three d^{IP} responses at 0.3 ms with the depth weighting. To form a sensitivity matrix, we used true σ_∞ model. Figure 30(a), (b) and (c) correspondingly show the recovered pseudo-chargeability sections from the 3D IP inversions of d^{IP} responses for σ_1 , $2 \times \sigma_1$, and $0.5 \times \sigma_1$ cases. Here we did not use the positivity constraint on $\tilde{\eta}$ in the inversion. Without any residual field, the recovered pseudo-chargeability is imaged on reasonable location as shown in Figure 30(a). With some residual fields due to the perturbed σ_1 , recovered pseudo-chargeability model include some artefacts. Due to the over-estimated d^{IP} ($2 \times \sigma_1$), we have minus residual fields. In this case, the recovered pseudo-chargeability model show positive artefacts spread on broad region. In contrast, for the under-estimated d^{IP} case, which has plus residual fields, the recovered model show negative artefacts. Even with regional fields, the recovered pseudo-chargeability still suggests proper geometric information of the IP body. In addition, by the definitions of the w^e and $\tilde{\eta}$ (equations (40) and (43)), the recovered pseudo-chargeability model should be positive. To incorporate this a priori information in the inversion, we use the positivity constraint with the Projected Gauss Newton scheme (CITE). Figure 30(c) shows the recovered pseudo-chargeability section from the d^{IP} response with $0.5 \times \sigma_1$. Negative artefacts in the recovered models are removed due to the positivity constraint. In Figure 31, we plotted the observed and predicted data for this inversion as a function of sounding number. We could not fit the positive d^{IP} responses, whereas the negative response was fit. This suggests that we can omit certain portion of the residual fields using this positivity constraint. This constraint may not be effective for the overestimated case ($2 \times \sigma_1$), because negative d^{IP} responses can be explained by positive pseudo-chargeability.

In addition, the incorrect conductivity have an effect on the sensitivity function, because the reference electric field (\vec{e}^{ref}) is a function of σ_∞ . In order to test the effect of the incorrect conductivity on the sensitivity function, we used sensitivity function from the canonical model, and inverted d^{IP} response for the conductive case at 0.3 ms. Figure 32 compares the recovered

pseudo-chargeability models with the true and incorrect sensitivity function. Although they are not exactly same, both magnitude and geometric shape of the recovered pseudo-chargeability for the IP body are similar. Therefore, the effect of the incorrect conductivity for the sensitivity function may not be very sensitive.

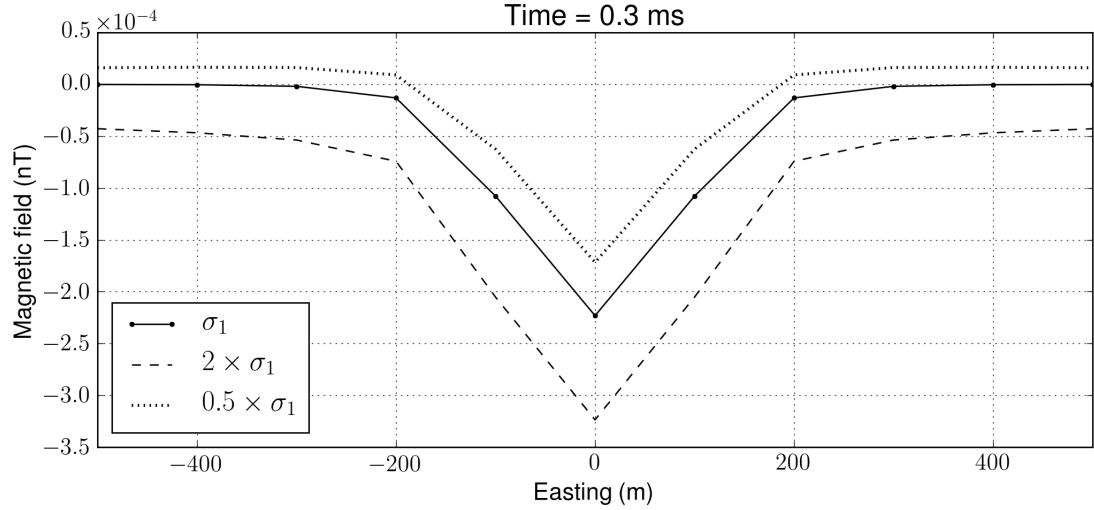


Figure 29: IP responses on a profile line at Northing -0 m. d^{IP} responses computed from

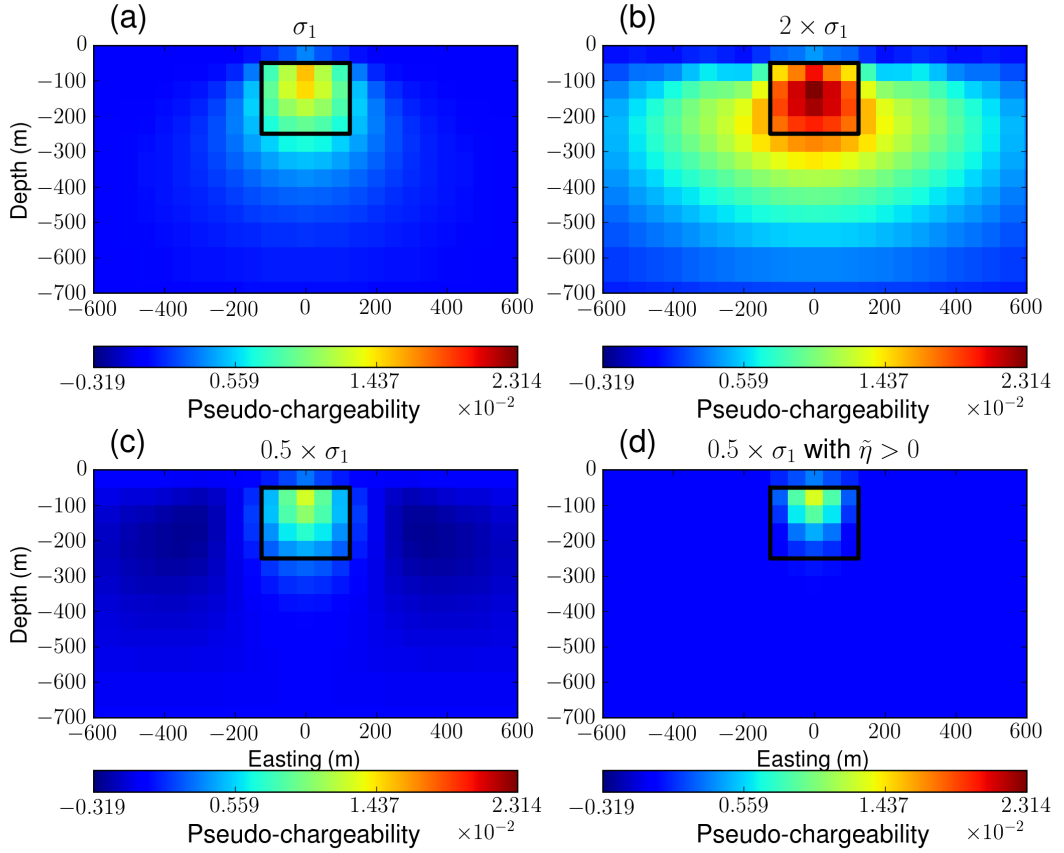


Figure 30: Recovered pseudo-chargeability sections from 3D IP inversions. (a) d^{IP} with true σ_1 . (b) d^{IP} with $2 \times \sigma_1$. (c) d^{IP} with $0.5 \times \sigma_1$. (d) d^{IP} with $0.5 \times \sigma_1$ and the positivity constraint on the pseudo-chargeability.

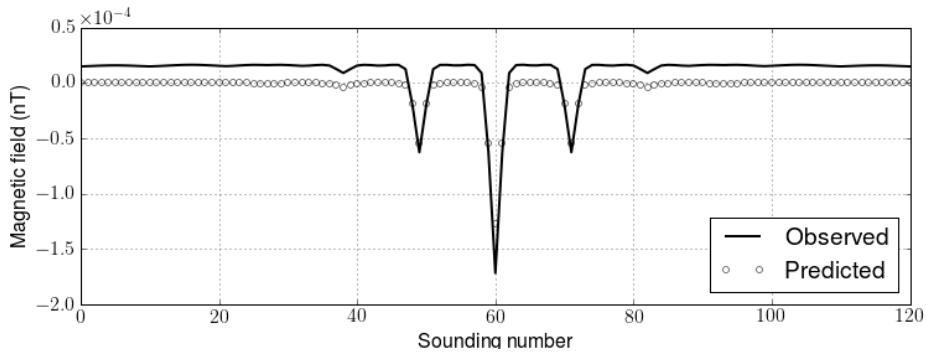


Figure 31: Comparison of the observed (solid line) and predicted (empty circles) data. d^{IP} response was generated with $0.5 \times \sigma_1$. The positivity constraint was used on $\tilde{\eta}$ for the 3D IP inversion.

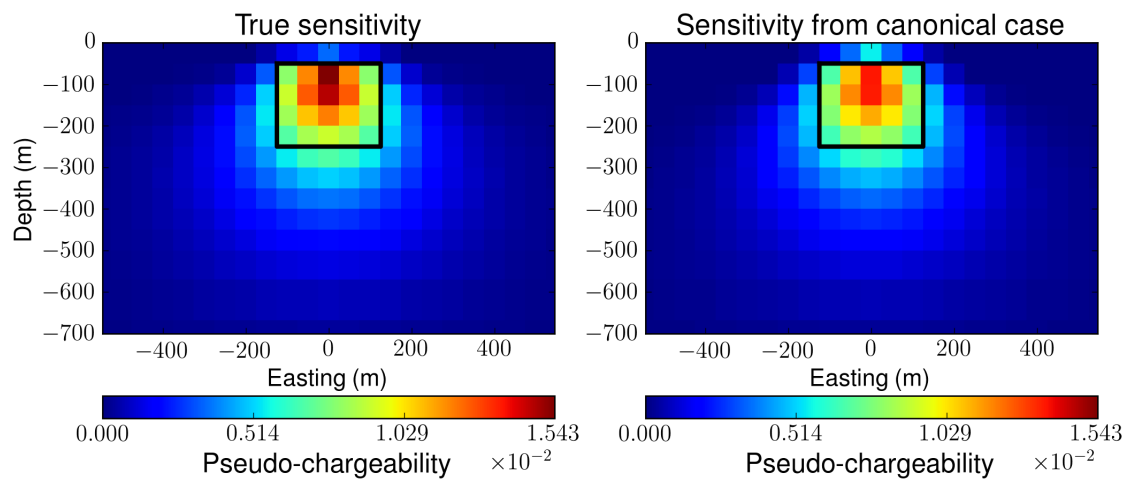


Figure 32: Recovered pseudo-chargeability sections from the 3D IP inversions for the conductive case. left and right show the inversion result from the true and incorrect sensitivity function. For the incorrect sensitivity we used conductivity model for the canonical case.

5.4.4 Extracting intrinsic IP parameters

Through two previous sections, we investigated three important aspects of our 3D IP inversion scheme: depth weighting, positivity constraint, and the effect of incorrect conductivity on sensitivity function. This composes the basis of the 3D IP inversion method for ATEM data thus, we will use the depth weighting and the positivity constraint. In addition, we showed that we can obtain geometry of the IP body from the recovered pseudo-chargeability model. However, as we recognized from the definition of the pseudo-chargeability (43), this is not intrinsic IP property, but convoluted property with $w^e(t)$, which is dependent on conductivity model. Therefore, we need to unravel this convoluted property to obtain intrinsic IP information from the recovered pseudo-chargeability model. There can be two issues for this task: a) how well we can recover the pseudo-chargeability model. b) deconvolution of the pseudo-chargeability to obtain intrinsic IP parameters. The first issue will have effect on the second one, because we need to recover reasonable pseudo-chargeability values to obtain intrinsic IP parameters from deconvolution.

To explore these issues, we first use approximate d^{IP} responses generated by linear kernel function. The averaged pseudo-chargeability on a single pixel in the IP body (Figure 24(b)) at an arbitrary time for all three cases is set to be constant in the IP body for all three cases. These equivalent pseudo-chargeability models are considered as true models (Figure 33). Due to the different averaged $w^e(t)$, three cases have different magnitude of the pseudo-chargeability. We generated approximate d^{IP} responses, ranging from 1 to 10 ms (14 channels), and recovered pseudo-chargeability model for each time channel. Figure 34a, show the recovered pseudo-chargeability sections for all three cases on the same scale with the true ones. Except for the conductive case, we underestimated the magnitude of the true pseudo-chargeability. To better recognize the geometry of the recovered models, we use relative scale on Figure 34b. Compared to the conductive case, two other cases has spreaded distribution of the IP body, which may result in underestimated pseudo-chargeability values. To extract of intrinsic IP parameters, we proceed deconvolution approach for the single pixel of the recovered pseudo-chargeability in the IP body (marked as white lines in the Figure 34b). Figure 35a and b show used $w^e(t)$ for the deconvolution and the recovered IP parameters, respectively. Note that true τ and η for all three cases are 0.005 and 0.2, respectively. For all three cases, recovered τ show reasonable match with the true one. The recovered η for the conductive case reasonable match with true one, whereas for two other cases η was underestimated due to the underestimated pseudo-chargeability.

Second, we apply the same procedure to the true d^{IP} response computed by the subtraction process (equation (26)). Used time range of d^{IP} is same as above (1-10 ms). Figure 36 show the recovered pseudo-chargeability sections for all three cases at 7.08 ms. The geometry of the recovered pseudo-chargeability model from the true d^{IP} responses show similar shape with the ones from the approximate d^{IP} responses (Figure 34b) for all three cases. We picked a single pixel in the IP body for all three cases, which is marked as white lines, then proceed deconvolution approach using the averaged $w^e(t)$ at that pixel. Figure 37a and b show used $w^e(t)$ for the deconvolution and the recovered IP parameters, respectively. Similar to the approximate d^{IP} case, the recovered τ are coincident to the true one. The recovered η show good match with the true one, whereas those for two other cases are underestimated. Recalling our assumption for the IP current did not work well for the resistive case in terms of the magnitude of the IP current (Figure 17), this is promising result that we can still recover reasonable geometry of the IP body and the time constant (τ). In addition, the conductive case that we can restore compact IP body may have more chance to recover intrinsic IP parameters.

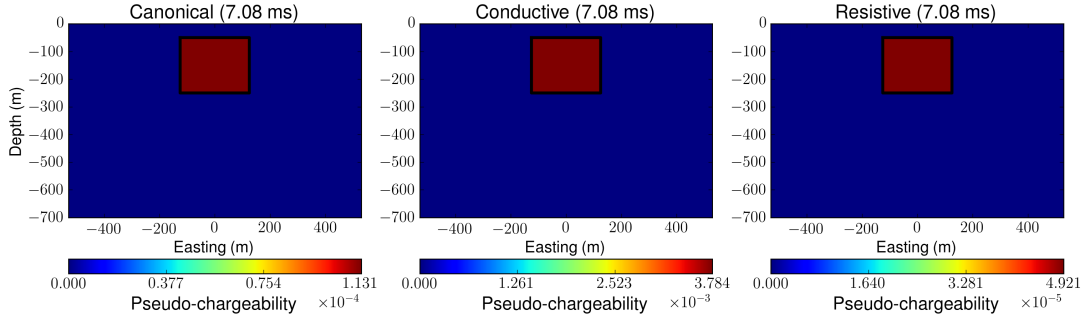


Figure 33: True equivalent pseudo-chargeability sections for three cases: canonical (left), conductive (middle), and resistive (right) IP models.

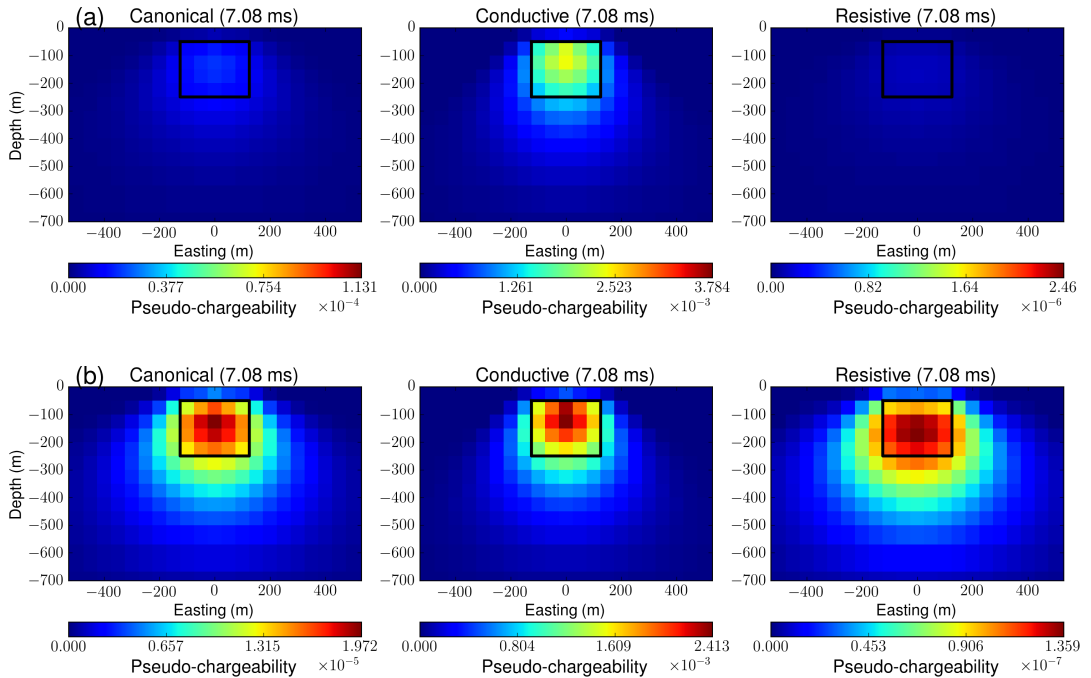


Figure 34: Estimated pseudo-chargeability sections for three cases: canonical (left panel), conductive (middle panel), and resistive (right panel) IP models by inverting approximate d^{IP} responses. (a) Same scale with true models. (b) Relative scale. White lines of rectangles indicate a certain pixel of the pseudo-chargeability model, which will be used to extract intrinsic IP parameters.

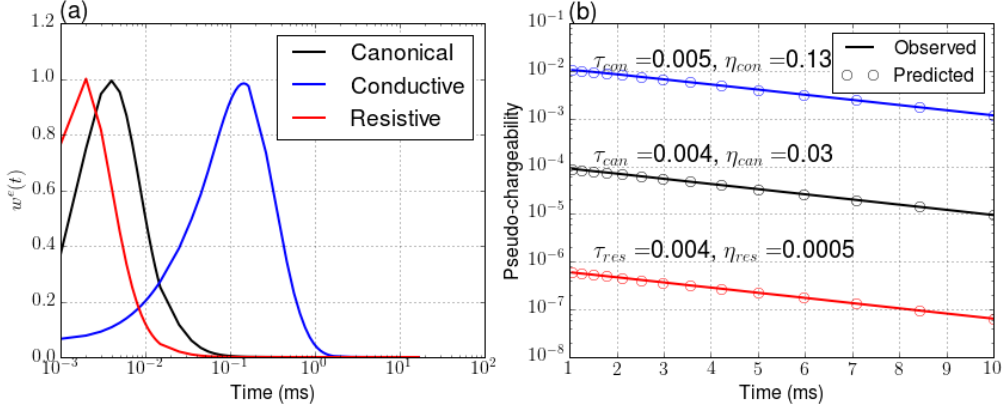


Figure 35: (a) The averaged $w^e(t)$ at a single pixel in the IP body (marked as white lines in Figure 34b) for all three cases. Black, blue and red colors correspondingly indicate canonical, conductive and resistive cases. (b) Comparisons of the observed (line) and predicted (empty circles) pseudo-chargeability at (0m, 0m, -125m) for three cases. Subscripts: can, con and res correspondingly stand for canonical, conductive and resistive cases.

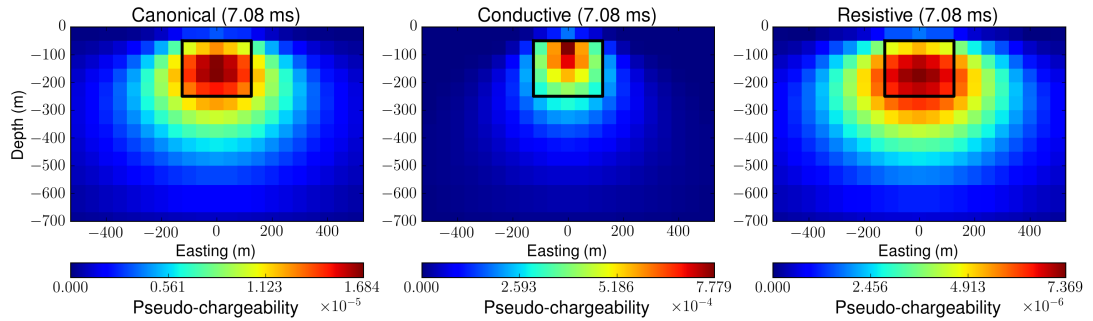


Figure 36: Estimated pseudo-chargeability sections for three cases: canonical (left panel), conductive (middle panel), and resistive (right panel) IP models by inverting true d^{IP} responses.

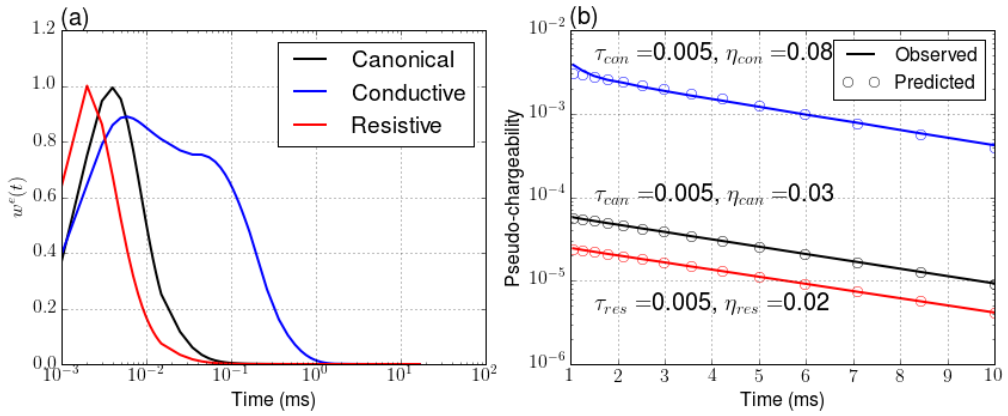


Figure 37: (a) The averaged $w^e(t)$ at a single pixel in the IP body (marked as white lines in Figure 36) for all three cases. Black, blue and red colors correspondingly indicate canonical, conductive and resistive cases. (b) Comparisons of the observed (line) and predicted (empty circles) pseudo-chargeability at (0m, 0m, -125m) for three cases. Subscripts: can, con and res correspondingly stand for canonical, conductive and resistive cases.

References

- [1] Jiuping Chen and Douglas W. Oldenburg. 3-D inversion of magnetic induced polarization data. *ASEG Extended Abstracts*, 2003(1):1–11, January 2003.
- [2] Kenneth S. Cole and Robert H. Cole. Dispersion and absorption in dielectrics i. alternating current characteristics. *The Journal of Chemical Physics*, 9(4), 1941.
- [3] Andreas Hördt, Tilman Hanstein, Mark Höning, and Fritz Manfred Neubauer. Efficient spectral IP-modelling in the time domain. *Journal of Applied Geophysics*, 59(2):152–161, June 2006.
- [4] David Marchant, Eldad Haber, and Douglas W. Oldenburg. Three-dimensional modeling of ip effects in time-domain electromagnetic data. *GEOPHYSICS*, 79(6):E303–E314, 2014.
- [5] D. Oldenburg and Y. Li. Inversion of induced polarization data. *GEOPHYSICS*, 59(9):1327–1341, 1994.
- [6] Partha S. Routh and Douglas W. Oldenburg. Electromagnetic coupling in frequency-domain induced polarization data: a method for removal. *Geophysical Journal International*, 145(1):59–76, 2001.
- [7] H. Seigel. Mathematical formulation and type curves for induced polarization. *GEOPHYSICS*, 24(3):547–565, 1959.
- [8] H. Seigel. The magnetic induced polarization (mip) method. *GEOPHYSICS*, 39(3):321–339, 1974.
- [9] Richard S. Smith, PW Walker, BD Polzer, and G. F. West. The time-domain electromagnetic response of polarizable bodies: an approximate convolution algorithm. *Geophysical Prospecting*, 36(April):772–785, 1988.
- [10] Yuval and D. Oldenburg. Computation of colecole parameters from ip data. *Geophysics*, 62(2):436–448, 1997.